AIMS Mathematics

AIMS Mathematics, 11(5): 14374–14411.
DOI: 10.3934/math.2026590
Received: 31 March 2026
Revised: 26 April 2026
Accepted: 28 April 2026
Published: 21 May 2026

https://www.aimspress.com/journal/Math

Research article

An intelligent prediction method for blasting craters of cylindrical blastholes based on Wavelet-Augmented Physics-Informed Neural Networks

Ting Zhu[1,2], **Hongyu Zhang**[1,2], **Yongsheng Jia**[1,2], **Yingkang Yao**[1,2], **Fan Yong**[3], **Nan Jiang**[1,2] **and Jinshan Sun**[1,2,*]

[1] State Key Laboratory of Precision Blasting，Jianghan University, Wuhan, 430056 Hubei, China
[2] Hubei Key Laboratory of Blasting Engineering, Jianghan University, Wuhan 430056, Hubei, China
[3] Key Laboratory of Hydroelectric Engineering Construction and Management in Hubei Province, Three Gorges University, Yichang, Hubei 443002, China

* **Correspondence:** Email: sunjinshan@jhun.edu.cn.

Abstract: Blasting crater prediction is critical for optimizing charge design and ensuring safety in engineering practice; however, traditional theoretical models suffer from idealized assumptions, numerical simulations are hindered by empirical parameter calibration and high computational cost, and physical experiments are constrained by scalability and repeatability. To address these challenges, a novel Wavelet-Augmented Physics-Informed Neural Networks (WA-PINNs) framework for accurately and efficiently predicting the diameter and volume of blasting craters induced by cylindrical charges is proposed. By leveraging Starfield's superposition method to equivalently model cylindrical charges as a series of spherical sources, a partial differential equation (PDE) system governing the tensile stress field responsible for crater formation was established. Comprehensive validation against high-fidelity numerical simulations and field experiments at Baima Iron Mine demonstrated that the WA-PINNs (Dog) achieves superior accuracy in predicting crater diameter and volume compared to conventional PINNs, with relative errors as low as 0.01 and markedly reduced training time. The results confirmed that the proposed WA-PINNs (Dog) is a robust, efficient, and physics-consistent intelligent solution for complex blasting problems, offering significant potential for real-world blasting design optimization.

Keywords: physics-informed neural networks; wavelets; blasting crater; charge mass; charge burial depth
Mathematics Subject Classification: 74-xx

1. Introduction

In practical blasting engineering, the complex geological environments and significant variations in mechanical parameters of natural rock masses pose considerable challenges to investigating rock fragmentation characteristics and optimizing blasting design schemes [1]. As a crucial window for understanding blasting-induced rock breakage mechanisms, research on the formation mechanism and geometric characteristics of blasting craters can provide effective engineering guidance for complex blasting operations, prompting studies on this topic by scholars at home and abroad [2,3].

Research on the scope of blasting craters domestically and internationally mostly employs three approaches: theoretical calculation, numerical simulation, and experimental investigation. In terms of theoretical calculation, Wang et al. [4] derived a formula for calculating the bottom radius of blasting craters by applying theories related to explosion shock waves and stress waves, along with their propagation and reflection laws in rock media. However, theoretical calculations exhibit notable limitations: They often rely on idealized assumptions (e.g., homogeneous rock mass and regular charge geometry) that seldom align with the complex and heterogeneous nature of natural rock masses encountered in practice, resulting in significant discrepancies between predicted outcomes and actual blasting effects. In the realm of numerical simulation, Ning et al. [5] simulated the complete formation process of blasting craters, reproducing phenomena such as borehole expansion, rock mass failure, fragment ejection, and muck pile formation. Yan et al. [6] examined the propagation and reflection of stress waves, identifying reflective tensile fracture on free surfaces as a key mechanism in crater formation. Zhang et al. [7,8] conducted discrete element method (DEM)-based simulations of blasting craters under varying charge burial depths, revealing that rock damage intensifies with shallower burial depths. Wang et al. [9–11] analyzed the dynamic tensile fracture behavior of rocks under explosive loading using the Taylor–Chen–Kuszmaul (TCK) continuum damage model. Zhu et al. [12–14] simulated crack propagation in blasting craters at different burial depths and determined the optimal charge burial depth. Nevertheless, numerical simulation suffers from two major shortcomings: First, the selection of constitutive models and parameter calibration heavily rely on empirical knowledge, and inaccurate parameter settings can compromise the reliability of results; second, it remains challenging to fully capture the complex coupled physical and mechanical behaviors during blasting (e.g., dynamic variation of gas pressure, interaction between crack propagation, and stress waves). Regarding experimental research, Ye et al. [15] performed single-hole blasting crater experiments at different burial depths and established a relationship between crater volume and burial depth. Although experimental results are generally reliable, this approach also has clear drawbacks: Constraints related to test conditions, equipment, and costs often restrict experiments to small-scale models, which are subject to scaling effects and cannot be directly extrapolated to real engineering scenarios. Additionally, experimental outcomes are susceptible to human interference and environmental variability, leading to poor repeatability in some cases, which complicates data analysis and generalization.

Neural network-based approaches have achieved significant progress in the field of intelligent computing. Conventional neural network methods are typically regarded as data-driven black-box models [16,17]. Using optimizers to minimize a loss function, these models learn underlying patterns from large-scale datasets associated with physical phenomena and engineering outcomes, thereby enabling efficient prediction of unknown physical behaviors and key characteristics based on the trained black-box representations. For instance, Hojjat et al. [18] incorporated a large set of experimental measurements of nanofluid temperature fields into an artificial neural network (ANN), establishing a relationship between temperature and thermal conductivity. Hung et al. [19] trained a neural network using structural acceleration response spectra under different seismic intensities; by integrating wavelet analysis for data filtering, they developed a rapid ANN-based method to assess building structural health under strong dynamic excitations. Nevertheless, purely data-driven conventional neural networks, which do not incorporate physical principles, are often criticized for their limited interpretability [20]. Their predictions may lack a rigorous mathematical-physical foundation and often fail to reveal explicitly expressible physical patterns.

The introduction of the Physics-Informed Neural Network (PINN) approach effectively incorporates physical information derived from governing equations into conventional neural networks, thereby enhancing their interpretability [21–23]. PINNs employ automatic differentiation within the network architecture to compute differential terms of the governing equations. By constructing a composite loss function that incorporates residuals from the governing equations, boundary conditions, initial conditions, and observational or experimental data, physical constraints are integrated into the learning process [24–26]. Through the use of suitable optimizers, the neural network is trained to minimize this loss function, effectively assimilating physical laws and measured data. Moreover, PINNs have undergone rapid development and have been successfully applied to a wide range of physical problems, including fluid dynamics [27], fluid-structure interaction [28], and interfacial crack analysis [29]. A notable advantage of PINNs is their capability to directly address inverse problems without requiring implicit solution schemes [30]. By treating the unknown parameters as outputs of the network and minimizing a loss function defined by the residuals of the governing equations and available constraints, a PINN can be trained end-to-end to reliably infer these parameters.

Despite these advancements, the application of PINNs to the modeling of blasting craters remains largely unexplored. The formation of a blasting crater involves complex multi-physics interactions, dynamic fracture propagation, and heterogeneous material behavior; processes that are challenging to capture accurately with conventional numerical or empirical methods. PINNs offer a promising framework for integrating blast-specific governing equations and initial/ boundary conditions into a unified learning process. PINNs have gained prominence as a mesh-free methodology for solving differential equations. However, their efficacy substantially declines when applied to problems characterized by high gradients, rapid oscillations, or singular behaviors, largely attributable to difficulties in balancing multiple loss components and accurately evaluating derivatives via automatic differentiation. Several strategies to mitigate these issues have been proposed in studies. For instance, McClenny et al. developed Self-adaptive PINNs (SA-PINNs) [31], which utilize trainable weighting parameters to dynamically adjust loss contributions. Concurrently, Wang et al. introduced a computationally practical PINN framework tailored for multi-scale problems with multi-magnitude loss terms (MMPINN) [32], integrating specialized neural architectures and regularization techniques. Although these approaches exhibit enhanced performance, they remain constrained by the computational burden associated with automatic differentiation and necessitate meticulous tuning of hyperparameters. Moreover, intelligent optimization methods integrated with physical constraints have been widely used in dynamic path planning and autonomous navigation [33,34]. Similarly, the WA-PINNs framework proposed in this paper embeds blasting mechanics into neural networks, which provides a new paradigm for intelligent prediction of blasting craters. The Wavelet-Augmented PINNs (WA-PINNs) framework proposed in this study presents an efficient alternative by representing the solution as a linear combination of wavelet basis functions. Rather than directly approximating the solution, WA-PINNs optimizes the expansion coefficients, thereby obviating the need for automatic differentiation in derivative computation, as the required derivatives can be analytically derived from the predefined wavelet bases. This methodology not only substantially reduces computational overhead but also inherently accommodates multi-scale phenomena and facilitates balanced loss term optimization. Therefore, extending WA-PINN methodologies to blasting crater analysis is not only a logical step in advancing physics-informed machine learning, but also holds significant potential for improving the predictability and optimization of blasting designs in engineering practice.

The remainder of this paper is structured as follows: In Section 2, we describe the physical mechanism underlying the blasting crater range calculation model for cylindrical blasting holes. In Section 3, we offer a detailed analysis of conventional PINNs and the novel WA-PINNs proposed in this study. In Section 4, a series of computational results are presented, demonstrating the advantages of the improved method. Finally, we conclude with a summary and outline prospects for future work.

2. Physical mechanism: Calculation model for blasting crater range of cylindrical blasting holes

2.1. Calculation model for blasting load

The accurate calculation and effective application of explosive loads remain the core challenge in the development of high-fidelity blasting simulation models. The constitutive relationship of the detonation process forms the theoretical foundation for the establishment of the borehole wall pressure-time history model, which decomposes the blasting process into four stages: (1) Pressure surge induced by detonation, (2) initial elastic expansion of the borehole, (3) crack propagation and subsequent gas infiltration into the cracks, and (4) medium fragmentation and gas venting. Consequently, this model is an indispensable tool for transforming the complex chemo-mechanical coupling effects of detonation into a computable load function.

In numerical simulations, the borehole pressure curve described above can be approximated through the following three methodologies: 1) Equation of State (EOS); 2) Pressure decay function; and 3) Direct imposition of time-varying dynamic pressure functions. In this investigation, we adopt the second approximation strategy, namely the pressure decay function approach. This methodology not only preserves physical fidelity but also establishes a differentiable and parameterized load trajectory for subsequent implementation of PINN. Such formulation effectively mitigates loss errors arising from inaccuracies in load input characterization.

To achieve this objective, a pressure decay function of the following form is adopted as the foundation for the load model:

$$F(t) = \frac{e^{-at}}{e^{-at}+e^{-bt}}, \tag{1}$$

where t represents time, with $a > 0,\ b > 0$. This function effectively captures the temporal characteristics of blast loading; namely, a rapid rise followed by a gradual decay. To the parameters a and b, the following constraint conditions are established based on the physical process of blasting pressure evolution:

1) At $t = 0$，$F = 0$: Substituting $t = 0$, there exists $F(0) = 0$, which holds universally without imposing additional constraints.

2) At $t = x$, F reaches its maximum value and remains positive, where $F^{'}(x) = 0$ and $F(x) = 0$.

3) At $t = y$, $F \approx 0.01 \times F(x)$. Namely, $\dfrac{F(y)}{F(x)} \approx 0.01$.

4) $y > x > 0$.

Under the maximum value condition, the following Eqs (2) and (3) can be derived:

Take the derivative of Eq (1) with respect to t :

$$F'(t) = (a + \frac{b}{2\sqrt{t}})e^{at+b\sqrt{t}} + ae^{-at}. \tag{2}$$

At $t = x, F'(x) = 0$:

$$(a + \frac{b}{2\sqrt{x}})e^{ax+b\sqrt{x}} + ae^{-ax} = 0. \tag{3}$$

The simplification assumes that the time duration of pressure rise is much shorter than the decay period, i.e., $x \ll y$. Under this condition, the higher-order exponential terms become negligible. Considering that the rise time x is typically two orders of magnitude smaller than the decay time y in blast loads, terms of order $e^{-b(y-x)}$ are neglected.

Since $e^{ax+b\sqrt{x}} \gg e^{-ax}$, the second term can be neglected, leading to:

$$a + \frac{b}{2\sqrt{x}} \approx 0, \tag{4}$$

$$b \approx -2a\sqrt{x}. \tag{5}$$

Based on Eqs (4) and (5), when $e^{b\sqrt{x}} \gg 1$ and $e^{b\sqrt{y}} \gg 1$, the following approximate solution (6) and (7) holds:

Given that the decay rate b is much larger than the initial rise rate a *(i.e.,* $|b| \gg |a|$, $t > 0$), the contribution of the term with $e^{b\sqrt{t}}$ becomes negligible compared to e^{at} in the numerator and denominator for the time range of interest.

$$F(x) \approx e^{ax+b\sqrt{x}}, \tag{6}$$

$$F(y) \approx e^{ay+b\sqrt{y}}. \tag{7}$$

Furthermore, based on the function condition, the following approximation can be derived:

$$a(y-x) + b(\sqrt{y} - \sqrt{x}) = \ln 0.01 = -\ln 100, \tag{8}$$

a and b can be derived by substituting Eq (3) into Eq (7) to replace b:

$$a = -\frac{\ln 100}{(\sqrt{y} - \sqrt{x})^2}. \tag{9}$$

From the pressure decay constraint $\frac{F(y)}{F(x)} \approx 0.01$, we derive:

$$a = -\frac{\ln 100}{(\sqrt{y} - \sqrt{x})^2} < 0. \tag{10}$$

Parameter a is always negative, which guarantees the monotonic decay of blast pressure over time, which is consistent with physical reality.

$$b = \frac{2\sqrt{x}\ln 100}{\sqrt{y} - \sqrt{x}}. \tag{11}$$

2.2. Stress field induced by a spherical cavity under load

We consider a spherical cavity of radius a_0 excavated in an elastic medium and filled with explosive material. During detonation, the cavity wall is subjected to a time-varying pressure load $p(t)$. The theoretical model is established based on the following fundamental assumptions:

(1) The cavity radius a_0 is sufficiently large and the charge mass is relatively small, such that the deformation of the cavity wall remains within the elastic range, thereby radiating elastic waves outward.

(2) The cavity is at a sufficient depth underground, enabling the influence of surface reflections on the elastic wave field to be neglected.

(3) The effect of initial in-situ stress is temporarily disregarded.

Due to the symmetry of the spherical coordinate system, all field variables depend only on the radial distance r from the center of the sphere and time t. The displacement component is unique and corresponds to the radial displacement $u(r,t)$.

Given that the decay rate b is much larger than the initial rise rate a (i.e., |b| ≫ |a|, $t > 0$), the contribution of the term with $e^{b\sqrt{t}}$ becomes negligible compared to in the numerator and denominator for the time range of interest. Expressed in terms of the potential function $\phi(r,t)$, the radial displacement $u(r,t)$ can be calculated by:

$$u(r,t) = \frac{\partial \phi}{\partial r}. \tag{12}$$

The stress components σ_r and σ_θ can be formulated by:

$$\begin{cases} \sigma_r = (\lambda + 2\mu)\dfrac{\partial u}{\partial r} + 2\lambda \dfrac{u}{r} \\ \sigma_\theta = \sigma_\varphi = \lambda \dfrac{\partial u}{\partial r} + 2(\lambda + \mu)\dfrac{u}{r} \end{cases}. \tag{13}$$

In Eq (13), λ and μ represent the Lamé constants. Owing to spherical symmetry in the spherical coordinate system, the tangential stresses in the θ and φ directions are equal; thus $\sigma_\theta = \sigma_\phi$. Eq (14) can be obtained by substituting Eq (12) to Eq (13):

$$\frac{\partial^2 (r\phi)}{\partial r^2} = \frac{1}{C_L^2}\frac{\partial^2 (r\phi)}{\partial t^2}, \tag{14}$$

where $C_L = \sqrt{(\lambda + 2\mu)/\rho}$ denotes the longitudinal wave velocity in the elastic medium with the intermediate substitution of the stress-strain relations.

After substitution and simplification, the Eq (15) can be obtained:

$$\phi(r,t) = \frac{1}{r} f\left(t - \frac{r}{C_L}\right). \tag{15}$$

The $\frac{1}{r}$ factor is correct for spherical waves in an elastic medium, representing geometric attenuation. We add a brief justification: "For a spherical wave propagating outward, the amplitude decays as $\frac{1}{r}$, which is consistent with the solution from $\phi = \frac{1}{r} f(t - \frac{r}{C_L})$.

By shifting the time argument to $\tau = t - \frac{r-a}{C_L}$, the wavefront arrives at radius r at time $t = \frac{r - a_0}{C_L}$. For $t < \frac{r - a_0}{C_L}$, the medium is undisturbed, automatically satisfying the zero initial conditions. This shift simplifies the boundary condition application at the cavity wall $r = a_0$, where $\tau = t$. To simplify the boundary and initial conditions, the variable $t - \frac{r - a_0}{C_L}$ is introduced to replace $\frac{t - r}{C_L}$ in Eq. (14), therefore $\phi(r,t)$ can be re-written as:

$$\phi(r,t) = \frac{1}{r} f(\tau). \tag{16}$$

Assuming the pressure direction as the positive direction, the initial and boundary conditions of the problem can be written as:

$$\sigma_r(a_0, t) = p(t),\ t > 0, \tag{17}$$

$$u(r,0) = 0, \dot{u}(r,0) = \frac{\partial u}{\partial t}|_{t=0} = 0 (r \geq a_0), \tag{18}$$

$$u(r,t) = \dot{u}(r,t) = 0, r \geq a_0. \tag{19}$$

Let $\tau = t - \frac{r}{C_L}$, then

$$\frac{\partial f(\tau)}{\partial r} = -\frac{1}{C_L} f'(\tau), \tag{20}$$

$$\frac{\partial^2 f(\tau)}{\partial r^2} = \frac{1}{C_L^2} f''(\tau). \tag{21}$$

Then substitute into the expression for σ_r to obtain terms proportional to $f''(\tau)$, $f'(\tau)$ and $f(\tau)$.

From Eqs (9), (10), and (13), the stress component σ_r are derived as:

$$\sigma_r = \frac{\lambda + 2\mu}{C_L^2 r} f''(\tau) + \frac{4\mu}{C_L r^2} f'(\tau) + \frac{4\mu}{r^3} f(\tau) \quad . \tag{22}$$

2.3. Parameter Equivalence for a cylindrical-to-spherical charge equivalence

In this investigation, starfield's superposition method is employed to equivalently represent a cylindrical charge utilizing a specific configuration of spherical charges. The core principle involves approximating the blasting effect of the cylindrical charge through the superposition of stress wave fields generated by a finite number of spherical charges of identical radius. The critical aspects of the superposition calculation include: (1) Spatially, the time delays of stress waves originating from spherical charges at different heights must be accounted for when they reach the target point; and (2) temporally, precise initiation timing control must be applied to each equivalent spherical charge to accurately replicate the actual detonation sequence within the cylindrical charge.

2.3.1. Equivalent spherical radius

When segmenting a cylindrical charge into a finite number of spherical charges of equal volume, it is essential to ensure that the centers of the equivalent spherical charges align with the axis of the cylindrical charge. Additionally, during this equivalent substitution, the total charge mass must remain unchanged despite the alteration in charge geometry. Subsequently, empirical formulas for calculating stress wave parameters of equivalent spherical charges are employed to determine the stress wave parameters induced by the extended charge under a given detonation wave velocity.

A schematic diagram of the cylindrical charge equivalently represented as a spherical charge is shown in Figure 1. Equation (23) can be calculated:

$$\frac{\pi d_c^2}{4} \cdot l = n \cdot \frac{4}{3} \pi r_b^3, \tag{23}$$

where r_b denotes the radius of the equivalent spherical charge, d_c represents the diameter of the cylindrical charge. From Eq (23), the relationship between r_b and d_c can be formulated by:

$$r_b = \frac{d_c}{\sqrt[3]{6}}. \tag{24}$$

The equivalent spheres are placed in contact along the charge axis, neglecting the small void spaces that would exist if spheres were exactly fitted into a cylinder. This approximation introduces a minor error in total charge volume (less than 5% for typical aspect ratios), which is acceptable for engineering predictions.

The number of equivalent spherical charges n can be calculated as:

$$n = \left(\frac{l}{2r_b}\right) = \frac{\sqrt{6}l}{3d_c}. \tag{25}$$

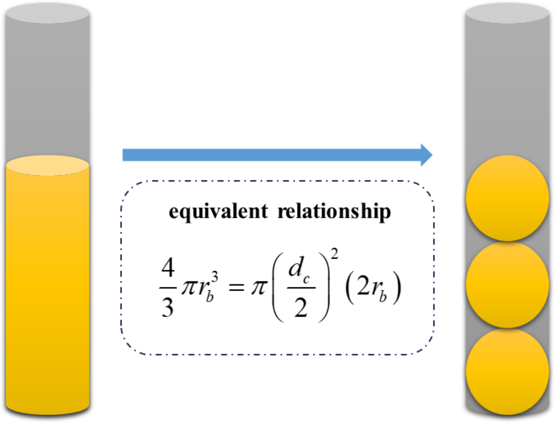

Figure 1. Division of equivalent charge.

2.3.2. Burden distance

For the equivalent spherical charge, the first charge starting from the closest free surface is numbered 1, and the remaining charges are numbered sequentially. Then, the burden length of the *i*-th charge in the blasthole perpendicular to the free surface is:

$$W_i = L + (2 \times i - 1) \times r_b, \tag{26}$$

where L denotes the stemming length measured from the top of the charge to the free surface (i.e., the distance from the uppermost equivalent sphere to the free face), and r_b represents the radius of the equivalent spherical charge.

2.4. The partial differential equation solution model for the blasting crater range

2.4.1. The formation condition of the blasting crater

The schematic diagram of the superposition of the incident wave and the reflected wave is shown in Figure 2. The stress calculation of the radial stress wave of the incident wave at p_0 in the direction perpendicular to the free surface σ_{ri1} is as follows:

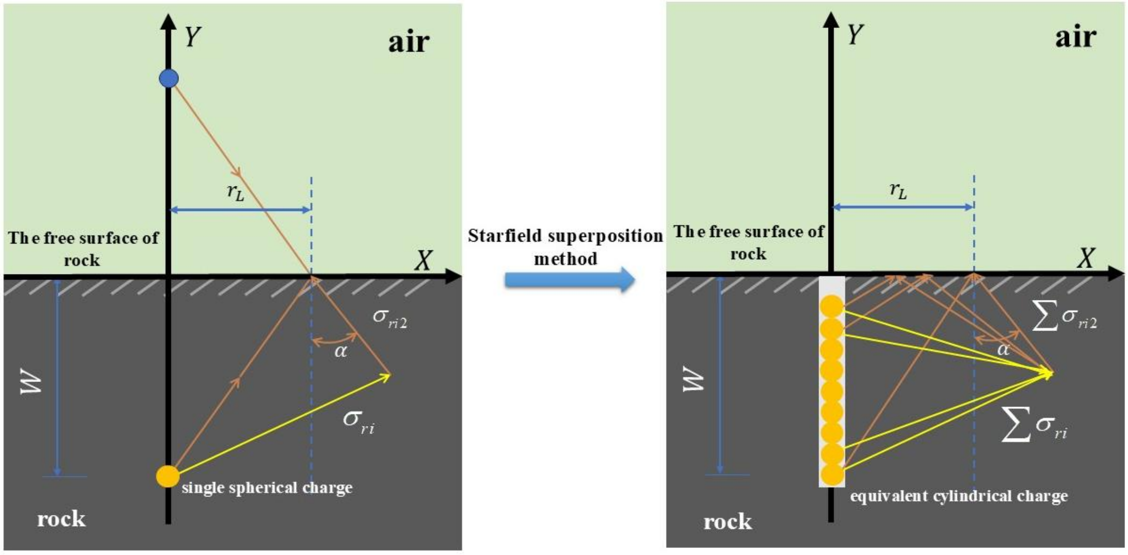

Figure 2. Schematic diagram of equivalent superposition of incident and reflected waves.

$$\sigma_{ri1}=\frac{|d-W_i|}{\sqrt{(d-W_i)^2+rl^2}}\sigma_{ri} \quad , \tag{27}$$

where σ_{ri} is the radial stress wave directly propagated from the i-th charge to p_0, and W_i is the burden of the i-th charge, which can be acquired from Eq (25). The travel distance r_i of the stress wave generated after the charge explosion to reach p_0 can be calculated by:

$$r_i=\sqrt{W_i^2+(r_l-x_i)^2}+\sqrt{x_i^2+d^2}. \tag{28}$$

The stress calculation of the radial stress wave of the stress reflected wave at p_0 in the direction perpendicular to the free surface σ_{ri2} can be obtained by:

$$\sigma_{ri2}=\frac{d}{\sqrt{x_i^2+d^2}}\sigma_{ri}R, \tag{29}$$

where R is the reflection coefficient. The reflection coefficient R is angle-dependent. For a P-wave incident on a free surface, $R=\frac{\cos^2 2\theta_s-(C_S/C_L)^2\sin^2 2\theta_s}{\cos^2 2\theta_s+(C_S/C_L)^2\sin^2 2\theta_s}$, where θ_s is the angle of the reflected shear wave. In this simplified model, we use the normal-incidence approximation $R\approx 1$ for tensile stress reversal.

The travel distance r_i of the stress wave generated after the charge explosion reaching point p_0 after reflection can be calculated by:

$$r_i=\sqrt{W_i^2+\left(r_l-x_i\right)^2}+\sqrt{x_i^2+d^2}\ . \tag{30}$$

The variable x_i is the horizontal distance from the point p_0 to the reflection point on the free surface. The dimensional consistency is now clear.

$$x_i = \frac{d \times r_i}{W_i + d}. \tag{31}$$

Equation (29) assumes a perfectly planar free surface such that the reflected wave appears to originate from an image source at a distance W_i behind the free surface, leading to an additional path length of $2W_i$ compared to the direct wave. The radial stress of the i-th spherical charge of both waves at p_0 can be obtained from Eq (17). The incident wave and the reflected wave are respectively calculated as:

$$\sigma_{ri} = \frac{\lambda + 2\mu}{C_L^{\,2} r_i} f''(\tau_i) + \frac{4\mu}{C_L r_i^2} f'(\tau_i) + \frac{4\mu}{r_i^3} f(\tau_i), \tag{32}$$

$$\sigma_{ri2} = \frac{\lambda + 2\mu}{C_L^{\,2} r_{i2}} f''(\tau_{i2}) + \frac{4\mu}{C_L r_{i2}^{\,2}} f'(\tau_{i2}) + \frac{4\mu}{r_{i2}^{\,3}} f(\tau_{i2}). \tag{33}$$

When a cylindrical charge is equivalent to multiple spherical charges, the tensile stress σ_y at a certain point in the rock perpendicular to the free surface can be formulated by combing Eqs (32) and (33) in the following:

$$\sigma_y = \sum \sigma_{ri1} + \sum \sigma_{ri2}. \tag{34}$$

Equation (34) assumes linear elastic superposition, which is valid for stress waves below the yield strength of the rock. Under plastic deformation or nonlinear rock behavior, superposition would not hold directly; however, the tensile failure criterion (Eq (35)) is applied only at the moment of crack initiation where strains are small. For highly nonlinear regimes, a more sophisticated damage model would be required. The formation condition of the blasting crater is that the sum of the tensile stresses at a certain point in the rock is greater than the tensile strength at that point, namely:

$$\sigma_y > \sigma_{td}, \tag{35}$$

σ_{td} is the dynamic tensile strength, which is rate-dependent. In this study, we adopt a simplified rate-dependent model: $\sigma_{td} = \sigma_{t0} \cdot (\dot{\epsilon}/\dot{\epsilon}_0)^{\alpha}$, where σ_{t0} is the static tensile strength, $\dot{\epsilon}$ is the strain rate, $\dot{\epsilon}_0$=1s^{-1}, and $\alpha = 0.33$ for typical rocks.

2.4.2. Establishment of the partial differential equation for solving the blasting crater

According to Eqs (17)–(19) and (22), it is known that to solve the stress, a solution of $f(\tau)$ needs to be established, which can be substituted from Eq (22) into Eq (20):

$$f''(\tau) + 2\xi f'(\tau) + (\xi^2 + \eta^2) f(\tau) = \frac{a_0}{\rho} p(\tau). \tag{36}$$

Using the relationships between Lamé constants and elastic parameters:

$$\lambda = \frac{E\nu}{(1+\nu)(1-2\nu)}, \tag{37}$$

$$\mu = \frac{E}{2(1+\nu)}. \tag{38}$$

Substitute into the wave equation coefficients and simplify to obtain:

$$\xi = \frac{1-2\nu}{1-\nu} \cdot \frac{C_L}{a_0}, \tag{39}$$

$$\eta = \frac{\sqrt{1-2\nu}}{1-\nu} \cdot \frac{C_L}{a_0}. \tag{40}$$

where ν denotes the Poisson's ratio of the rock medium.

In this way, the solution of the integral function is converted into the solution of the partial differential equation, which is subject to the following initial conditions:

$$u(r,t) = \dot{u}(r,t) = 0. \tag{41}$$

The boundary conditions are given by:

$$\sigma_r(a_0,t) = p(t), t > 0. \tag{42}$$

2.5. Applicability and limitations of the model assumptions

(1) Elastic spherical cavity assumption: This is valid when the charge mass is relatively small and the rock behaves elastically before fracture. For large-scale blasting with significant plasticity, the model may underestimate crater size; we suggest incorporating a plasticity correction factor in future work.

(2) Neglect of in-situ stress: The model is suitable for shallow or surface blasting where in-situ stress is negligible. For deep tunnel blasting, in-situ stress should be considered; a qualitative correction formula is provided.

(3) Ignoring surface reflection effects on stress wave superposition: This assumption holds when the blasting point is sufficiently far (>10 m) from the free surface; for very shallow burial depths (<1 m), the simplified reflection coefficient may introduce errors.

3. Wavelet-augmented physics-informed neural networks for a blasting crater range calculation model

3.1. Physics-informed neural networks (PINNs)

A neural network is a mathematical framework composed of layered neurons interconnected through nonlinear transformations. Its architecture typically comprises an input layer for receiving data, multiple hidden layers for hierarchical feature extraction, and an output layer for generating predictions. According to the universal approximation theorem, a neural network with sufficient hidden layers and neurons can approximate any continuous function with arbitrary accuracy [35]. The information flow between layers follows a structured transformation process:

Input layers:

$$z^0 = x \in \mathbb{R}^{n_0}. \tag{43}$$

Hidden layers:

$$z^k = \sigma(\omega^k z^{k-1} + b^k), 1 \le k \le L-1. \tag{44}$$

Output layers:

$$z^L = \omega^L z^{L-1} + b^L \in \mathbb{R}^{n_L}. \tag{45}$$

where $z^k \in R^{n_k}$ represents the output of the k-th layer, $\omega^k \in R^{n_k \times n_{k-1}}$ denotes the weight matrix, $b^k \in R^{n_k}$ is the bias vector, and n_k indicates the number of neurons in the k-th layer. Parameters ω and b are optimized during training, while σ represents a nonlinear activation function. This computational procedure is conventionally referred to as feed-forward propagation.

The network's performance is evaluated through a loss function L that quantifies the discrepancy between predicted and target values. Training is performed via backpropagation, which employs gradient-based optimization algorithms to minimize the loss function by adjusting model parameters (ω, b). Through this process, the network learns to capture the underlying patterns in the data.

A notable variant of this framework is physics-informed neural networks (PINNs), which integrate physical constraints by incorporating governing equations, initial conditions, and boundary conditions into the loss function. The composite loss function is formulated as $L = L_{res} + L_{ic} + L_{bc}$, where L_{res} measures the residual error of the governing equations, while L_{ic} and L_{bc} quantify errors in initial and boundary conditions, respectively. The optimization process requires computing derivatives of the loss function with respect to model parameters and the network output with respect to inputs, which are efficiently evaluated using automatic differentiation [36].

Consequently, PINNs aim to determine parameter values that minimize the composite loss function, thereby satisfying the physical constraints embedded in the training objective.

3.2. Wavelet-augmented physics-informed neural networks (WA-PINNs)

The WA-PINNs formulation begins with a family of wavelets constructed through dilations and translations of a mother wavelet function. For a given mother wavelet $\psi(x)$, the dilated and translated wavelet functions for integer scale and shift parameters $j, k \in \mathbb{Z}$ are defined as:

$$\Psi_{j,k}(x) = \sqrt{2}j \cdot \psi(2^j x - k), \tag{46}$$

where j denotes the dilation exponent and represents the translation parameter. To specify the number of wavelet family members, we fix a resolution set J. For each $j \in J$, the translation parameter k ranges from $\lceil a \cdot 2^{j+1} \rceil$ to $\lceil b \cdot 2^{j+1} \rceil$, where $\lceil \cdot \rceil$ denotes the ceiling function. This construction ensures that the domain $[a, b]$ is covered across resolution levels. Using this wavelet family, the solution of the differential equation is approximated as:

$$\hat{u}(x)=\sum_{j=J_1}^{J_N}\sum_{k=[a\cdot 2^{j+1}]}^{[b\cdot 2^{j+1}]} c_{j,k}\Psi_{j,k}(x)+\mathcal{B}, \tag{47}$$

where $\mathcal{B}$ is a bias term, J denotes the $i-th$ resolution level, and N is the total number of resolutions in the set J. Although each wavelet basis function $\Psi_{j,k}$ has zero mean, the solution may have a non-zero average component (e.g., a constant background stress). The bias term $\mathcal{B}$ is added to represent this constant offset, which cannot be captured by a linear combination of zero-mean wavelets alone. This ensures the completeness of the basis for functions with non-zero mean. This formulation can be readily extended to higher-dimensional problems. For a two-dimensional case, the wavelet basis function is defined as:

$$\Psi_{j_1,j_2,k_1,k_2}(x,y)=\sqrt{2}j\cdot 2^{j_2}\cdot\psi_X(2^{j_1}x-k_1)\psi_Y(2^{j_2}y-k_2), \tag{48}$$

and the approximate solution becomes:

$$\hat{u}(x,y)=\sum_{j_1=J_{11}}^{J_{1N_1}}\sum_{j_2=J_{21}}^{J_{2N_2}}\sum_{k_1=[a_1\cdot 2^{j_1+1}]}^{[b_1\cdot 2^{j_1+1}]}\sum_{k_2=[a_2\cdot 2^{j_2+1}]}^{[b_2\cdot 2^{j_2+1}]} c_{j_1,j_2,k_1,k_2}\Psi_{j_1,j_2,k_1,k_2}(x,y)+\mathcal{B}, \tag{49}$$

where the domain $\Omega=[a_1,b_1]\times[a_2,b_2]$ is discretized using resolution parameters J_1 and J_2 corresponding to the x and y dimensions, respectively. The translation parameters k_1 and k_2 define the positioning of basis functions along these respective dimensions. This hierarchical construction of wavelet families at different resolutions enables capturing solution features at multiple scales-from broad, global behavior to fine, local details. In this study, three mother wavelets are considered, namely, Complex Morlet function $\psi^C(x)$, the Paul function $\psi^P(x)$, and the Dog function $\psi^D(x)$. The mathematical expressions for the three mother wavelets can be written as:

$$\psi^C(x)=\pi^{-1/4}e^{i\omega_0 t}e^{-t^2/2}, \tag{50}$$

$$\psi^P(x)=(1-it)^{-(m+1)}, \tag{51}$$

$$\psi^D(x)=e^{-t^2/(2a^2)}-k\cdot e^{-t^2/(2b^2)}. \tag{52}$$

The architecture of WA-PINNs is illustrated in Figure 3. For the partial differential equation in Eq (36), the loss function L is given by

$$L=w_{res}L_{res}+w_{ic}L_{ic}+w_{bc}L_{bc}, \tag{53}$$

where

$$L_{res}=\frac{1}{N_u}\sum_{i=1}^{N_u}\left|f''(\tau_i)+2\xi f'(\tau_i)+\left(\xi^2+\eta^2\right)f(\tau_i)-\frac{a_0}{\rho}p(\tau_i)\right|^2, \tag{54}$$

$$L_{ic}=\frac{1}{N_m}\sum_{i=1}^{N_m}\left|f'(\tau_i)-f'(\tau=0)\right|^2+\frac{1}{N_m}\sum_{i=1}^{N_m}\left|f(\tau_i)-f(\tau=0)\right|^2, \tag{55}$$

$$L_{bc}=\frac{1}{N_b}\sum_{i=1}^{N_b}\left|\sigma_r(a_0,\tau_i)-p(\tau_i)\right|^2. \tag{56}$$

The solution of the differential equation (36) is approximated by the neural networks. L_{res} denotes penalization of the residuals of the differential equation, and L_{ic} and L_{bc} denote that of the initial and boundary conditions respectively. N_u, N_m, and N_b denote the number of collocation points used. w_{res}, w_{ic}, and w_{bc} are the weight coefficients corresponding to each loss item.

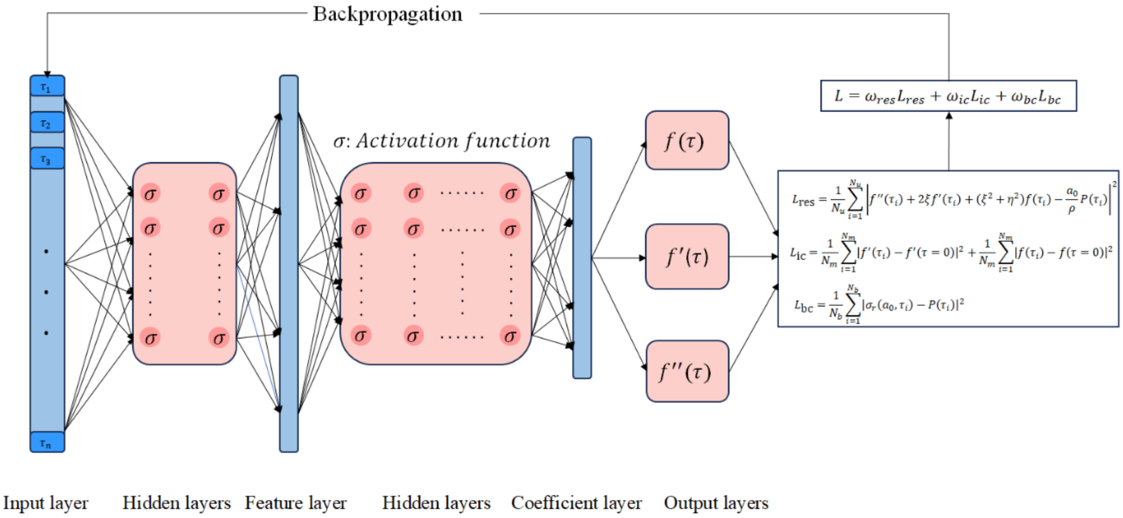

Figure 3. A WA-PINNs architecture.

3.3. WA-PINNs model verification for the wave equation solution of a spherical Charge

To validate the proposed WA-PINNs model, the following numerical example are considered. The corresponding physical parameters, charge parameters, and PINNs network parameters are displayed in Tables 1–3, respectively.

Table 1. Physical parameters of rock mass.

Rock density/$(kg\cdot m^{-3})$	Elastic modulus/GPa	Poisson's ratio	Rising time of pressure/s
2400	50	0.25	0.0001

Table 2. Charge parameters for numerical example.

Charge length/m	Charge diameter/m	Blasthole diameter/m	Charge density/ $(kg\cdot m^{-3})$	Detonation velocity /(m/s)	Isentropic exponent
3	0.1	0.1	1200	5500	1.3

Table 3. PINNs network parameters used in the numerical example.

Parameters	Value
Number of collocation points	104

Number of initial condition points	2000
Number of boundary condition points	400
Number of hidden layers	6
Number of epochs	104
Learning rate	10−3
Optimizer	Adam+L-BFGS-B
Activation function	tanh

The network architecture is designed with six hidden layers, each containing 128 neurons. The weights are initialized using Xavier uniform initialization, and full batch training is employed, meaning all collocation points are processed at the same time.

For training hyperparameters, the batch size is set to 512 for residual points and 256 for initial and boundary points. The learning rate starts at 10^{-3} and decays exponentially at a rate of 0.95 every 500 epochs. The optimization process uses the Adam optimizer for the first 5000 epochs, followed by the L-BFGS-B optimizer for fine-tuning.

The hyperparameters are selected based on the following considerations. The wavelet scales are chosen to cover the computational domain $[0,10]$ using a dyadic grid. The number of collocation points, set to 10^4, is determined through a sensitivity study, as the error is found to saturate when the number of points exceeds 8000. Learning rate decay is applied to prevent oscillations in the loss function during training.

Regarding wavelet expansion settings, the resolution levels are determined according to the frequency analysis of blast wave signals. A corresponding translation range is assigned for each resolution level. The mother wavelet is selected based on its time-frequency localization properties that match the characteristics of blast waves. Specifically, the fourth Dog wavelet is used, whose parameters are optimized for capturing the peak features of blast waves.

Figure 4 presents the calculated displacement results obtained by the five methods, namely Mathematica, PINNs, WA-PINNs (Complex Morlet), WA-PINNs (Paul), and WA-PINNs (Dog). Table 4 summarizes the error metrics and other performance evaluation indices for the four PINN-based methodologies, benchmarked against the analytical solution derived from Mathematica in the numerical test case presented in this section.

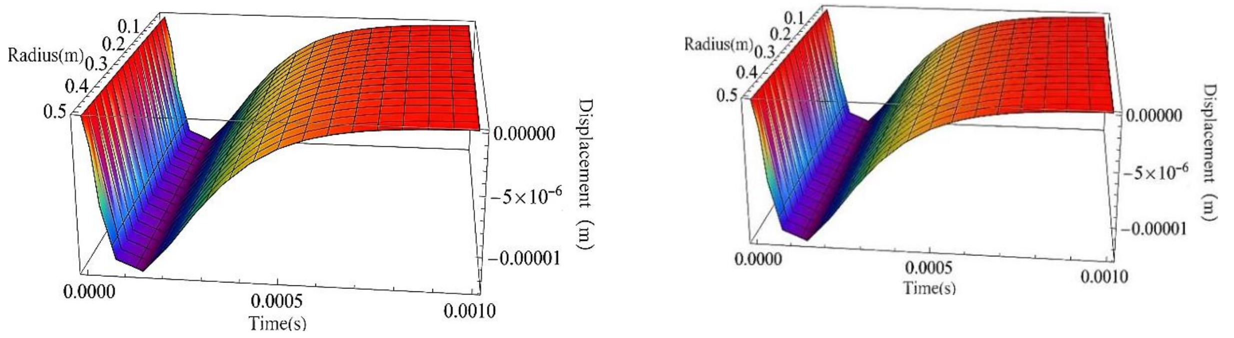

(a) Mathematica

(b) PINNs

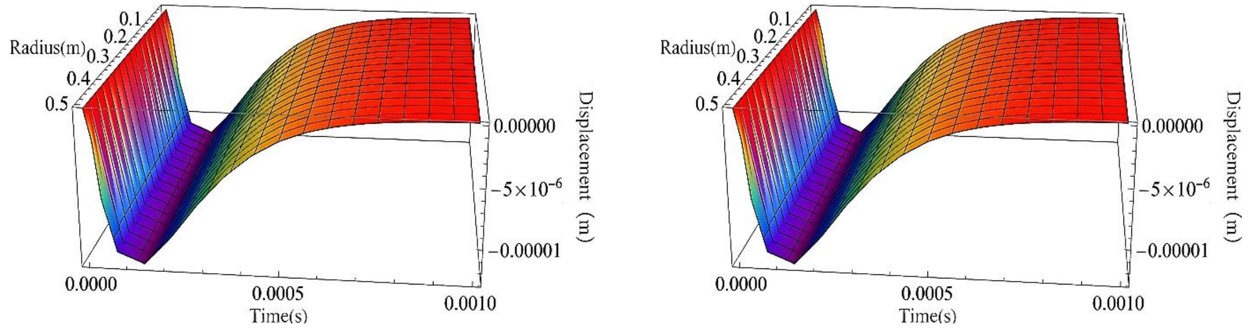

(c) WA-PINNs (Complex Morlet)

(d) WA-PINNs (Paul)

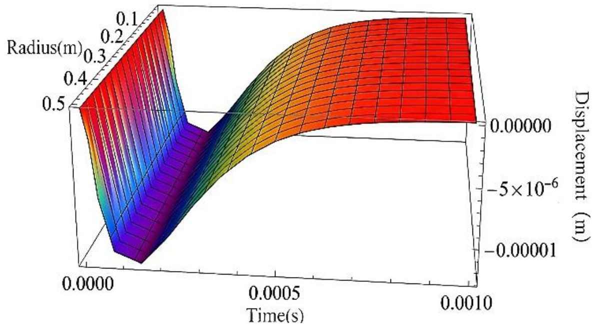

(e) WA-PINNs (Dog)

Figure 4. Comparison of displacement calculated by (a) Mathematica; (b) PINNs; (c) WA-PINNs (Complex Morlet); (d) WA-PINNs (Paul); and (e)WA-PINNs (Dog).

Table 4. Performance comparison for different models.

Model	Relative L^2 error	Training time (s)	Min absolute error	Max absolute error	Mean absolute error
PINNs	0.19	168.57	0.0016	0.0322	0.0031
WA-PINNs (Complex Morlet)	0.16	157.24	0.0007	0.0287	0.0035
WA-PINNs (Paul)	0.05	84.67	0.0009	0.0105	0.0026
WA-PINNs (Dog)	0.01	43.64	0.001	0.0051	0.0014

4. Experimental verification of the calculation model for blasting crater range

4.1. Experimental results of numerical simulations for blasting craters

4.1.1. Numerical simulation model

The model is mostly composed of rocks and explosives. Through trial calculations with different grid quantities, the grid quantity dependence is analyzed. Considering computational accuracy and efficiency comprehensively, the non-uniform discretization method is determined for element meshing. All model elements adopt linear triangular elements, with a total of 276,620 triangular elements and 47,224 nodes. The model dimensions are shown in Figure 5, with a length of 6 m, a width of 6 m, and a height of 4 m. The top surface of the model is set as a free boundary, while the surrounding and bottom surfaces are set as non-reflective boundaries. The coupling charging method is adopted between the charge and the rock mass, and the coupling effect between them is realized by defining the contact surface. For the grid elements of explosive and rock mass, defined contact surfaces are used to generate virtual interfaces inside the model to realize the subsequent rock fragmentation calculation.

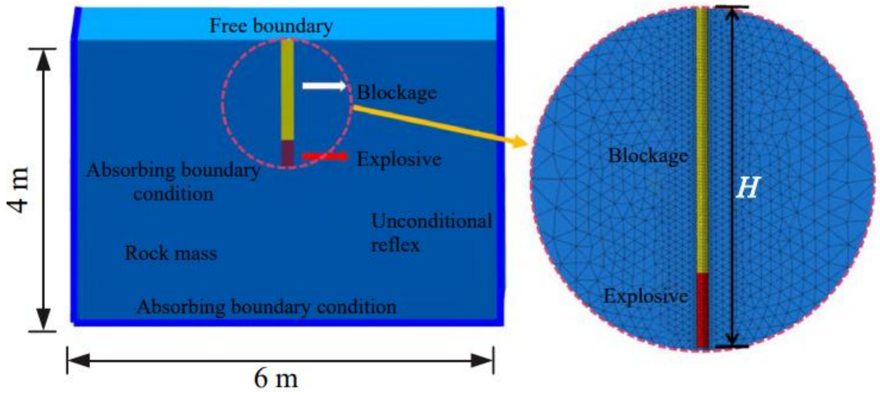

Figure 5. Numerical calculation model of a blasting crater.

4.1.2. Materials and parameters of the numerical simulation model

(1) Materials and parameters of the rock model

In numerical simulation calculations, the concept of virtual cracks is introduced, which are on the boundaries of each finite element. That is, virtual contact surfaces are constructed between rock elements. Before fracture occurs, the two sides of the solid element are connected by normal and tangential penalty springs to realize the transfer of mechanical information. After fracture occurs, the virtual contact surfaces are transformed into real contact surfaces, and corresponding contact parameters are assigned, thereby realizing the coupling between the finite element and the discrete element [37]. The contact surfaces adopt a fracture energy model. The material parameters of the rock model are taken as listed in Table 1, and the stiffness parameters of the contact surfaces are taken as listed in Table 5.

Table 5. Contact surface parameters.

Normal Stiffness/ (GPa·m^{-1})	Tangential Stiffness/ (GPa·m^{-1})	Tensile Fracture Energy/ (J·m^{-2})	Shear Fracture Energy/ (J·m^{-2})
2×10^5	2×10^5	100	1000

(2) Materials and parameters of explosive model

Since the composite mixed-medium emulsion explosive is adopted in this study, considering the calibration of calculation parameters and calculation efficiency, the Landau detonation source model is used for the explosive, and the parameters are taken according to Table 2. The input parameters of the Landau detonation model include charge density, detonation velocity of explosive, heat of detonation, and ignition point location. The model is mainly based on the Landau-Stanyukovich formula:

$$\begin{cases} p_a V_a^{\gamma} = p_0 V_0^{\gamma} & p_a \geq p_k \\ p_a V_a^{\gamma_1} = p_k V_k^{\gamma_1} & p_a < p_k \end{cases}, \tag{57}$$

where, $\gamma = 3$; $\gamma_1 = \frac{4}{3}$; P_a and V_a are the transient pressure and volume of the high-pressure gas sphere, respectively; P_0 and V_0 are the pressure and charge volume at the initial moment, respectively; and P_k and V_k are the pressure and charge volume of the high-pressure gas sphere at the boundary of the two adiabatic processes, respectively.

4.1.3. Numerical simulation results

(1) Different charge masses at fixed burial depths

Numerical simulation is conducted for experimental scheme A, and the blasting crater morphology and crater bottom diameter under different charge masses are obtained, with the results shown in Figure 6. It can be found from Figure 6 that the average diameter of the blasting crater bottom increases with the increase of charge mass. When the charge masses are 3, 4, 5, and 6 kg, the numerically simulated average diameters of the blasting crater bottom are 1.66, 2.76, 3.46, and 4.35 m, respectively.

(2) Different burial depths with fixed charge mass

In scheme B, the rock strength is higher than that in scheme A. Therefore, in the numerical simulation, the rock strength parameters are adopted as specified in Table 1. The results of the blasting crater morphology and crater bottom diameter under different charge burial depths in experiment scheme B are presented in Figure 7. It can be observed from Figure 7 that the diameter of the blasting crater bottom first increases and then decreases with the increase of charge burial depth. When the charge burial depths are 1.4, 1.6, 1.8, and 2.0 m, the numerically simulated average diameters of the blasting crater bottom are 3.54, 3.59, 3.03, and 2.39 m, respectively.

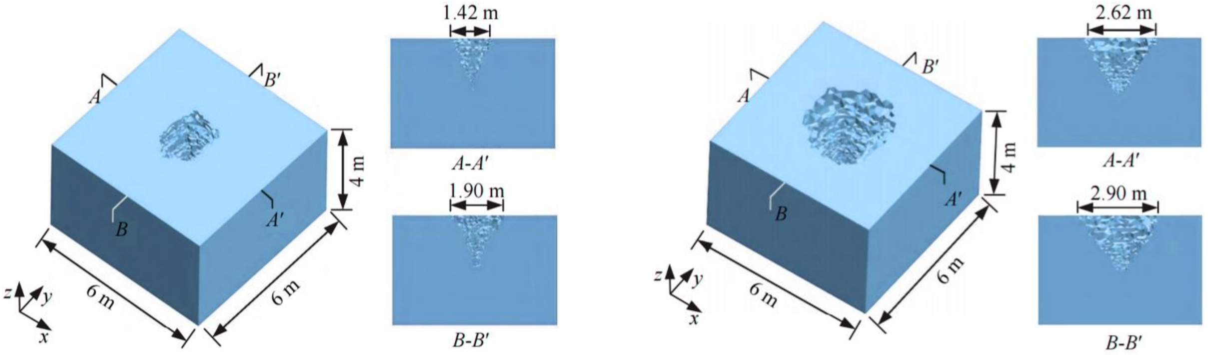

(a) Charge mass: 3 kg (b) Charge mass: 4 kg

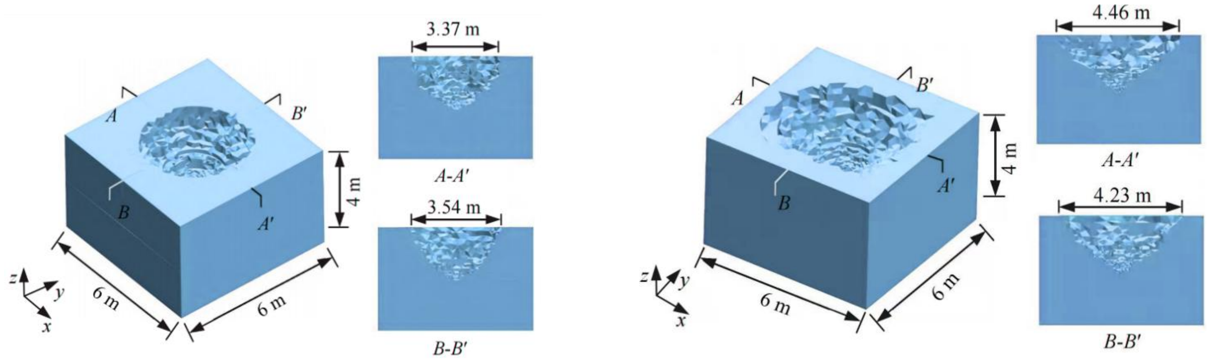

(c) Charge mass: 5 kg (d) Charge mass: 6 kg

Figure 6. Numerical simulation results under different explosive package weights (explosive burial depth is fixed at 2.0 m).

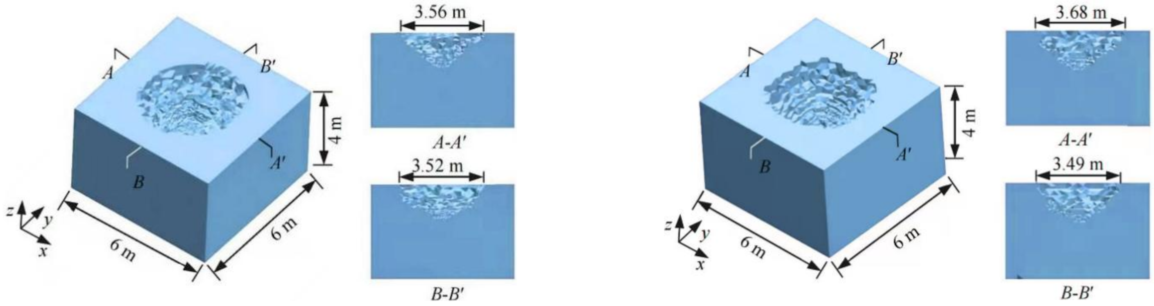

(a) Burial depth: 1.4 m (b) Burial depth: 1.6 m

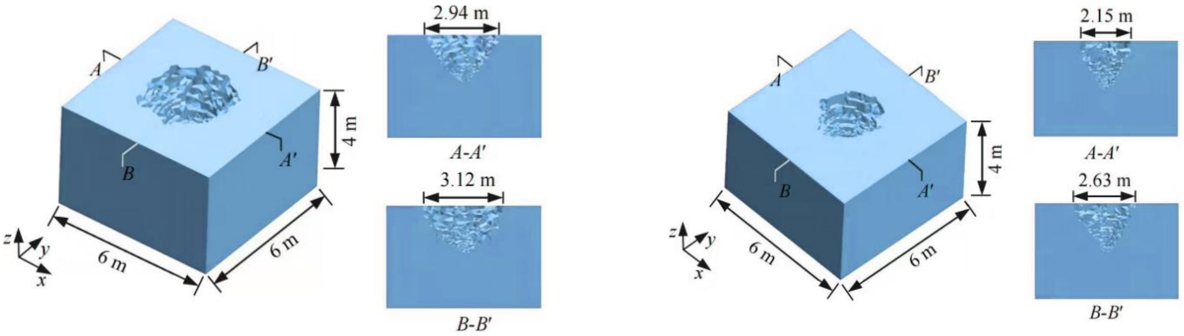

(c) Burial depth: 1.8 m (d) Burial depth: 2.0 m

Figure 7. Numerical simulation results under different explosive burial depths (explosive packet weight is fixed at 4 kg).

4.2. Field experimental results of the blasting crater

4.2.1. Experimental scheme

This experiment is in Baima Iron Mine, Baima Town, Miyi County, Panzhihua City, Sichuan Province. The rock mechanics parameters are shown in Table 6. A Type 2 rock emulsified explosive (squeezing coupling) is adopted, with a charging density of 1.15 g/cm³, and the explosive parameters are shown in Table 7. Experimental scheme A: The charge burial depth is fixed at 2.0 m, and the charge masses are 3, 4, 5, and 6 kg, respectively; Scheme B: The charge mass is fixed at 4 kg, and the charge burial depths are 1.4, 1.6, 1.8, and 2.0 m, respectively. In two groups of experiments, the blasthole diameter is 115 mm, and the charging height is 0.3 ~ 0.6 m. The field experiment is shown in Figure 8.

(a) Explosive cartridge (b) Charging

(c) Hole Layout (d) Charge Structure

Figure 8. Field experiments.

Table 6. Physico-mechanical parameters of rock mass.

Density/ (kg·m⁻³)	Elastic Modulus/ GPa	Poisson's Ratio	Internal Friction Angle/ (°)	Tensile Strength/ MPa	Dilatancy Angle/ (°)
2500	65.0	0.25	30.0	8	12.0

Table 7. Explosive parameters.

Density/ (kg·m^{-3})	Detonation Velocity/ (m·s^{-1})	Detonation Heat/ (J·kg^{-1})	Detonation Pressure/ GPa
1100	4800	3×10^{6}	7.0

4.2.2. Experimental results of scheme A

After detonation, the morphology of the blasting crater and the measured bottom diameter of the blasting crater are shown in Figure 9.

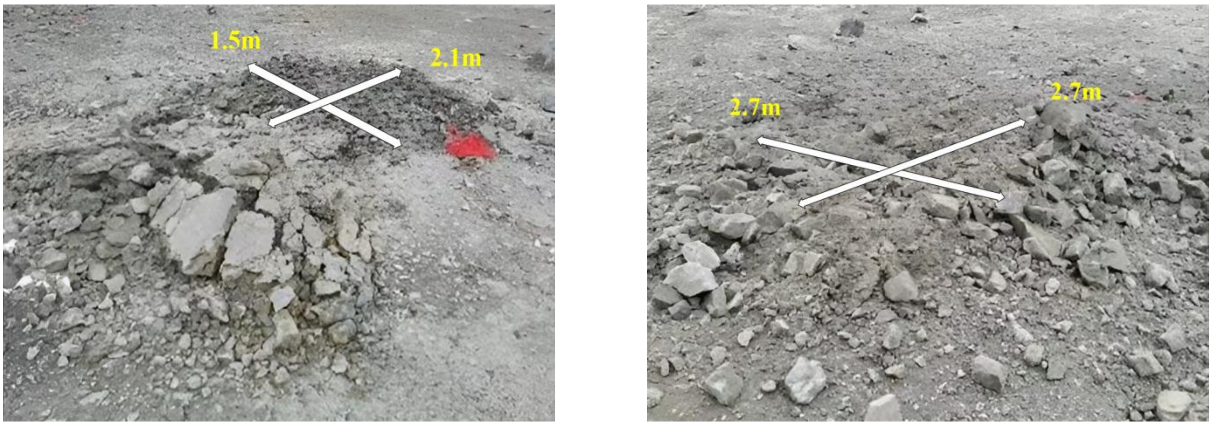

(a) Charge mass: 3 kg (b) Charge mass: 4 kg

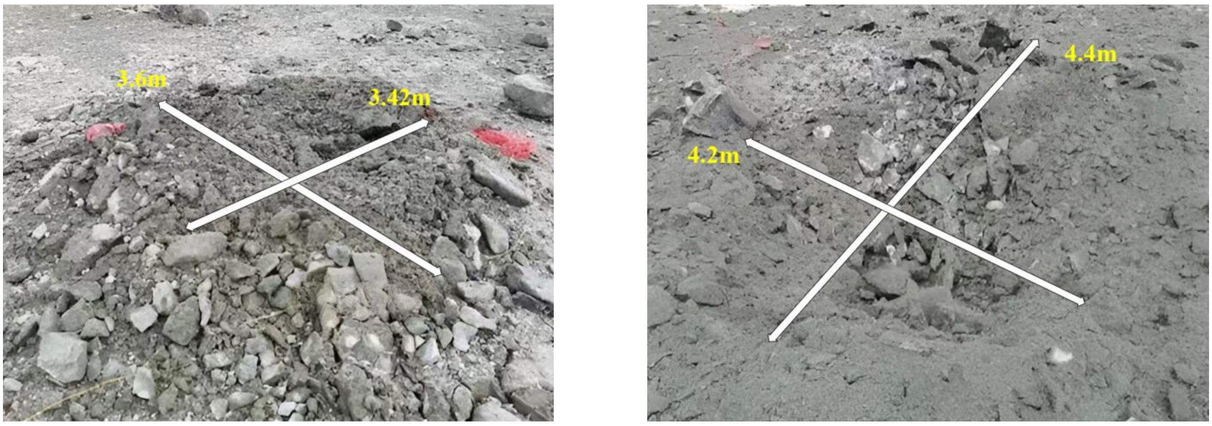

(c) Charge mass: 5 kg (d) Charge mass: 6 kg

Figure 9. Blasting crater under different explosive package weights (explosive burial depth is fixed at 2.0 m).

It can be seen in Figure 9 that when the charge mass is 3 kg, the average diameter of the blasting crater bottom is 1.80 m. When the charge mass increases to 4, 5, and 6 kg, the average diameter of the blasting crater bottom increases to 2.70, 3.51, and 4.50 m, respectively. The diameter of the blasting crater and the rock mass damage range increase with the increase of the charge mass, and the throwing and scattering distance of broken rock blocks also increases with the increase of the charge mass. To explain this phenomenon from the perspective of energy: As the charge mass increases, the total explosion energy increases, which will inevitably lead to a larger damage range of the rock mass and a farther throwing distance of rock blocks.

4.2.3. Experimental results of scheme B

According to on-site rock sample testing, the rock strength in experiment scheme B is higher than that in scheme A, with its rock mechanics parameters presented in Table 8. The morphology of the blasting crater and the measured bottom diameter of the blasting crater are illustrated in Figure 10.

Table 8. Physico-mechanical parameters of rock mass in scheme B.

Density/ (kg·m^{-3})	Elastic Modulus/ GPa	Poisson's Ratio	Internal Friction Angle/ (°)	Tensile Strength/ MPa	Dilatancy Angle/ (°)
2600	68.5	0.23	35.0	9.2	10.0

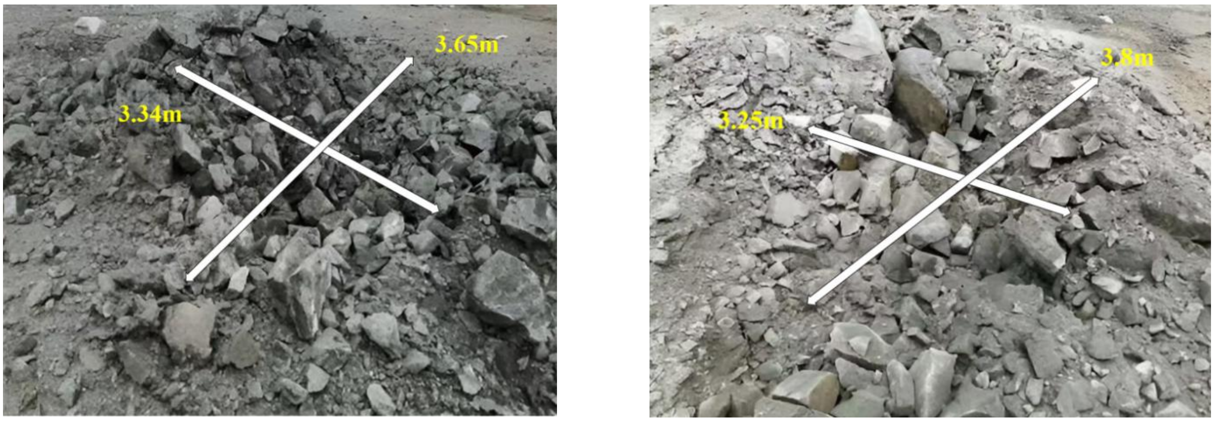

(a) Burial depth: 1.4m (b) Burial depth: 1.6m

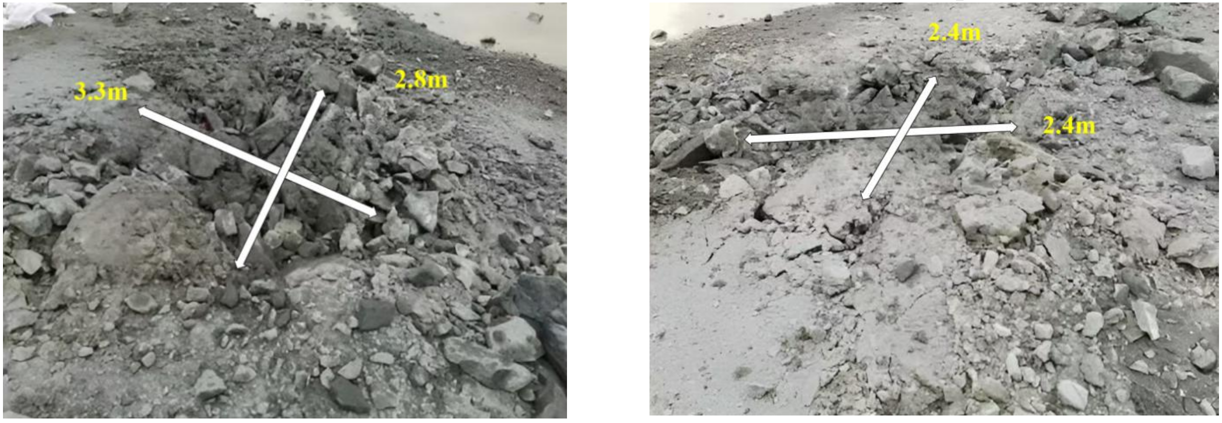

(c) Burial depth: 1.8 m (d) Burial depth: 2.0 m

Figure 10. Blasting funnel crater with different explosive burial depths (explosive packet weight is fixed at 4 kg).

It can be seen in Figure 10 that when the charge burial depth is 1.4 m, the average diameter of the blasting crater bottom is 3.49 m. When the charge burial depth increases to 1.6, 1.8, and 2.0 m, the diameters of the blasting crater bottom are 3.53, 2.8, and 2.4 m, respectively. The average diameter of the blasting crater bottom and the rock mass damage range first increase and then decrease with the increase of the charge burial depth, and the maximum average diameter of the blasting crater bottom occurs when the charge burial depth is 1.6 m. The throwing and scattering distance of broken rock blocks decreases gradually with the increase of the charge burial depth.

4.3. Experimental results of PINN-related methods

The PINN parameters are reported in Table 9. The loss function of four PINN-related methods is displayed in Figure 11 and the performance indices are stated in Table 10.

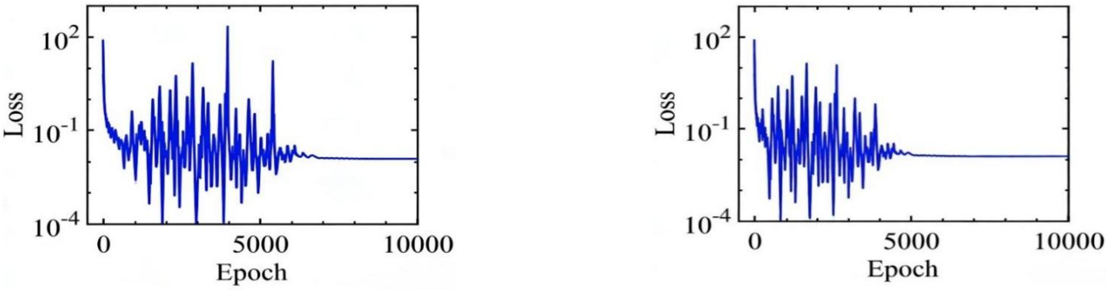

(a) PINNs (b) WA-PINNs (Complex Morlet)

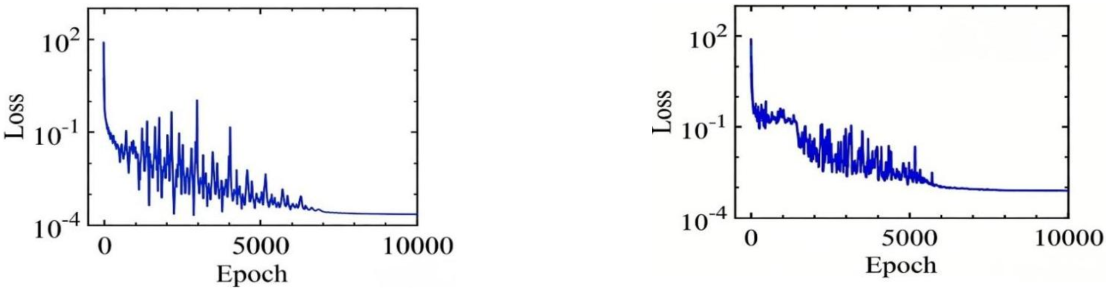

(c) WA-PINNs (Paul) (d) SA-PINNs

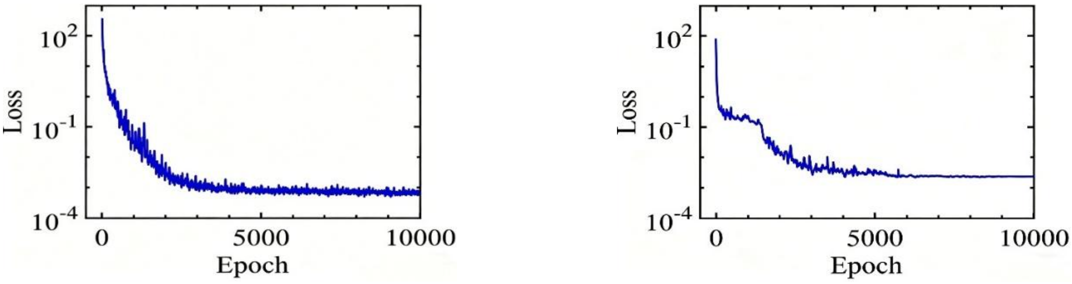

(e) MMPINNs (f) WA-PINNs (Dog)

Figure 11. Evolution of the loss across the epochs.

From Table 10, it is evident that WA-PINNs (Dog) have a more accurate prediction and takes significantly less training time.

Table 9. PINN parameters used in Section 4.3.

Parameters	Value
Number of collocation points	104
Number of initial condition points	2000
Number of boundary condition points	400
Number of hidden layers	6
Number of epochs	104
Learning rate	10−3
Optimizer	Adam+L-BFGS-B
Activation function	tanh

Table 10. Performance comparison of four models.

Model	Relative L^2 error	Total loss	Training time(s)	Min absolute error	Max absolute error	Mean absolute error
PINNs	0.59	375.18	128.67	0.26	21.58	9.11
WA-PINNs (Complex Morlet)	0.46	27.63	90.14	0.07	10.66	2.74
WA-PINNs (Paul)	0.15	10.57	121.42	0.18	9.59	0.88
SA-PINNs	0.23	19.45	187.34	0.13	15.82	3.33
MMPINNs	0.18	14.28	163.21	0.11	12.78	2.47
WA-PINNs (Dog)	0.01	0.04	55.79	0.05	4.39	0.54

4.4. Results: Comparisons and analyses

4.4.1. Prediction results of the diameters

To validate the forecasting performance of the proposed architecture, six models (numerical simulation, field experiment, PINNs, WA-PINNs (Complex Morlet), WA-PINNs (Paul), and WA-PINNs (Dog)) are selected for comparisons and analysis. Tables 11 and 12 and Figure 12 show the average diameter of six models for two schemes.

Table 11. The average diameters of blasting craters utilizing six methods in scheme A.

Charge mass	3kg	4 kg	5 kg	6 kg
Numerical simulation/(m)	1.660	2.760	3.460	4.350
Field experiment/(m)	1.800	2.700	3.510	4.500
PINNs/(m)	1.633	2.726	3.413	4.416
WA-PINNs (Complex Morlet) /(m)	1.683	2.734	3.489	4.285
WA-PINNs (Paul) /(m)	1.687	2.778	3.481	4.301
WA-PINNs (Dog) /(m)	1.667	2.752	3.469	4.374

Table 12. The average diameters of blasting craters utilizing six methods in scheme B.

Burial depth	1.4m	1.6m	1.8m	2.0m
Numerical simulation/(m)	3.540	3.590	3.030	2.390
Field experiment/(m)	3.490	3.530	2.800	2.400
PINNs/(m)	3.512	3.557	3.057	2.424
WA-PINNs (Complex Morlet) /(m)	3.527	3.566	3.054	2.405
WA-PINNs (Paul) /(m)	3.551	3.573	3.011	2.406
WA-PINNs (Dog) /(m)	3.544	3.592	3.024	2.383

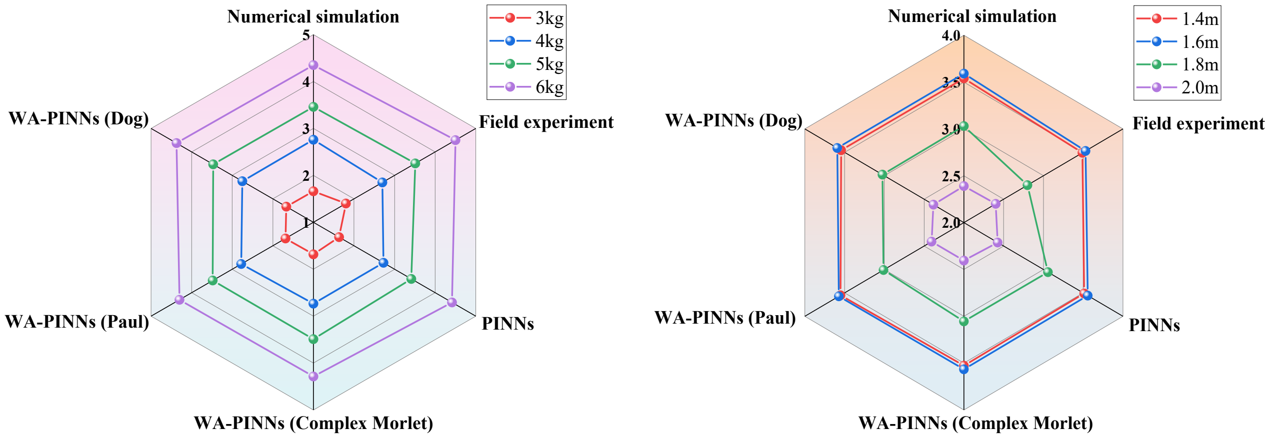

(a) Average diameter of scheme A (b) Average diameter of scheme B

Figure 12. The average diameters of two schemes.

Compared with the results of numerical simulations and field experiments, three error metrics, namely MAE, RMSE and MAPE, for the average diameter results derived from the four PINN-related methods are presented in Figures 13–16, respectively.

For the average diameter in scheme A, compared to the numerical simulation results, the MAE values of the four models, PINNs model, WA-PINNs (Complex Morlet) model, WA-PINNs (Paul) model, and WA-PINNs (Dog) model, are 0.0435 m, 0.0358 m, 0.0288 m, and 0.0120 m, respectively; the RMSE values are 0.0021 m, 0.0016 m, 0.0010 m, and 0.0002 m, respectively; and the MAPE values are 1.4335%, 1.1650%, 1.0030%, and 0.3809%, respectively. The maximum MAE, RMSE, and MAPE values do not exceed 0.045 m, 0.0022 m, and 1.17%, respectively. Among the four models, WA-PINNs (Dog) exhibits the optimal predictive performance.

Against the field experimental results for the average diameter in scheme A, the four models, PINNs, WA-PINNs (Complex Morlet), WA-PINNs (Paul), and WA-PINNs (Dog), yield MAE values of 0.0935 m, 0.09675 m, 0.10475 m, and 0.088 m; RMSE values of 0.014756 m, 0.005908 m, 0.003933 m, and 0.029848 m; and MAPE values of 3.9675%, 3.285%, 3.605%, and 3.3225%, respectively. None of the MAE, RMSE, and MAPE values exceed 0.11 m, 0.015 m, and 4%, respectively. Accordingly, the four models are ranked in descending order of predictive performance as follows: WA-PINNs (Complex Morlet) > WA-PINNs (Dog) > WA-PINNs (Paul) > PINNs.

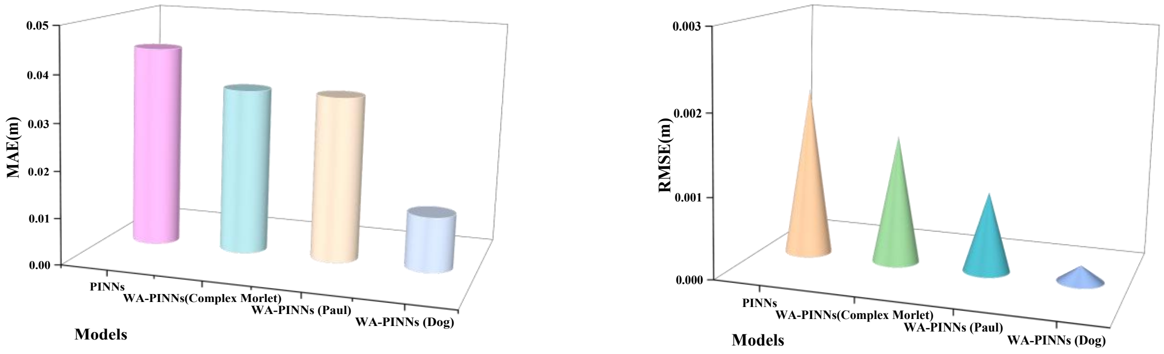

(a) MAE (b) RMSE

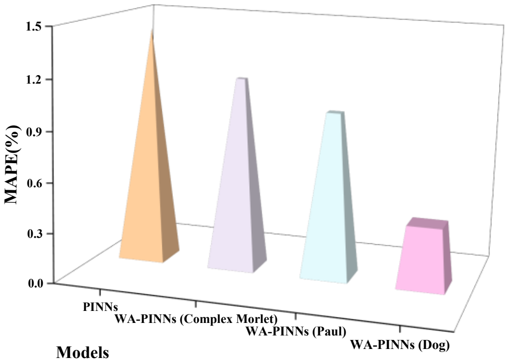

(c) MAPE

Figure 13. Prediction errors of the average diameters in scheme A compared with numerical simulations.

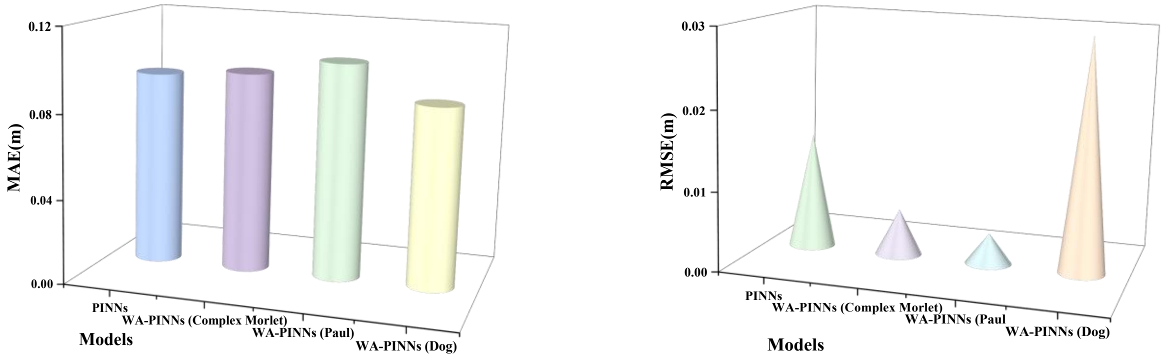

(a) MAE (b) RMSE

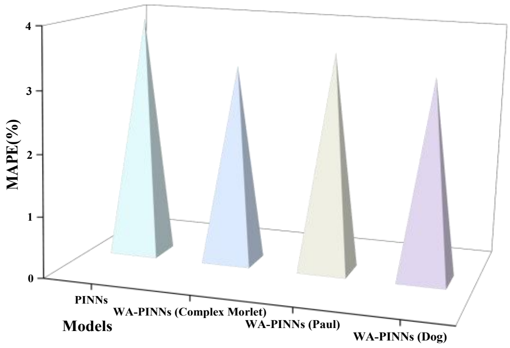

(c) MAPE

Figure 14. Prediction errors of the average diameters in scheme A compared with field experiments.

For the average diameter in scheme B, compared with the numerical simulation results (shown in Figure 15), the MAE values of the four models, namely the PINNs model, WA-PINNs (Complex Morlet) model, WA-PINNs (Paul) model, and WA-PINNs (Dog) model, are 0.0305 m, 0.0190 m, 0.01575 m, and 0.00475 m, respectively. The RMSE values are 0.03065 m, 0.01966 m, 0.01602 m, and 0.00512 m, respectively. The MAPE values are 1.0060%, 0.6139%, 0.5202%, and 0.1649%, respectively. The maximum MAE, RMSE, and MAPE values do not exceed 0.031 m, 0.031 m, and 1.01%, respectively, and among the four models. The WA-PINNs (Dog) exhibits the best prediction performance.

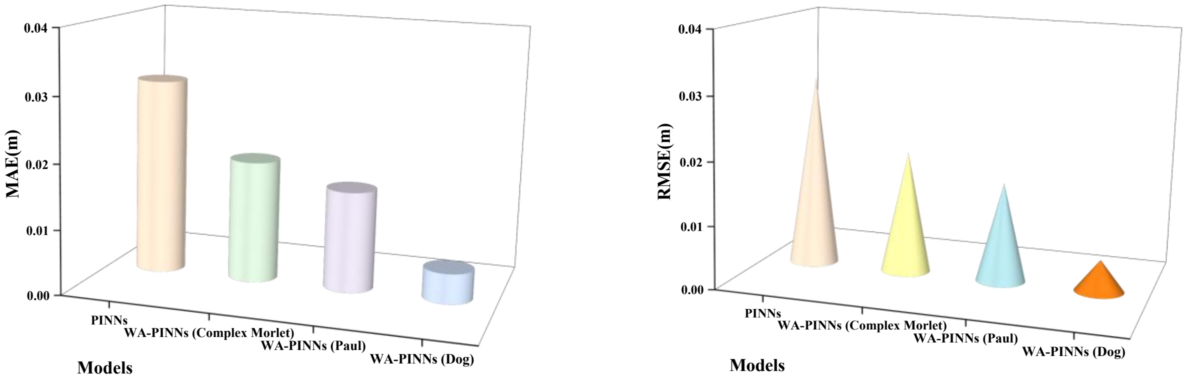

(a) MAE (b) RMSE

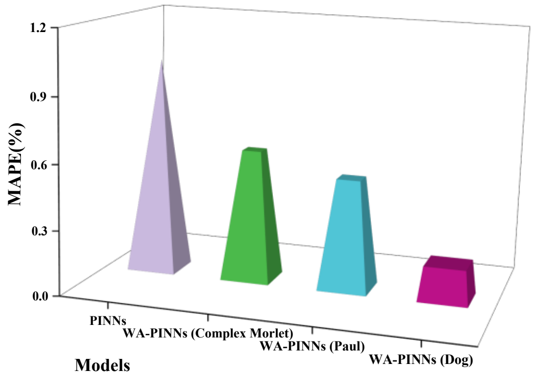

(c) MAPE

Figure 15. Prediction errors of the average diameters in scheme B compared with numerical simulations.

For the average diameter in scheme B, compared with the field experimental results (shown in Figure 16), the four models, PINNs, WA-PINNs (Complex Morlet), WA-PINNs (Paul), and WA-PINNs (Dog), exhibit MAE values of 0.089 m, 0.069 m, 0.058 m, and 0.055 m; RMSE values of 0.092 m, 0.070 m, 0.060 m, and 0.056 m; and MAPE values of 3.107%, 2.428%, 2.106%, and 1.943%, respectively. The maximum MAE, RMSE, and MAPE values do not exceed 0.09 m, 0.095 m, and 3.2%, respectively. The comparative results indicate that the predictive performance ranks as follows: WA-PINNs (Dog) > WA-PINNs (Paul) > WA-PINNs (Complex Morlet) > PINNs.

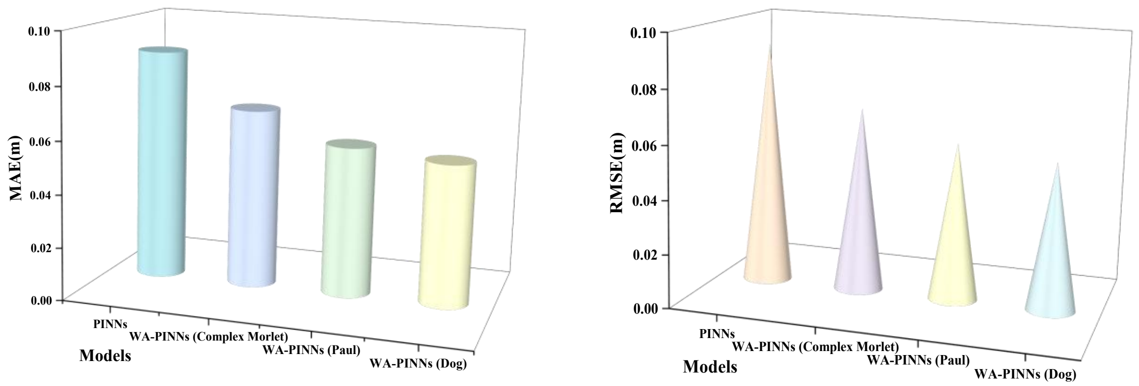

(a) MAE

(b) RMSE

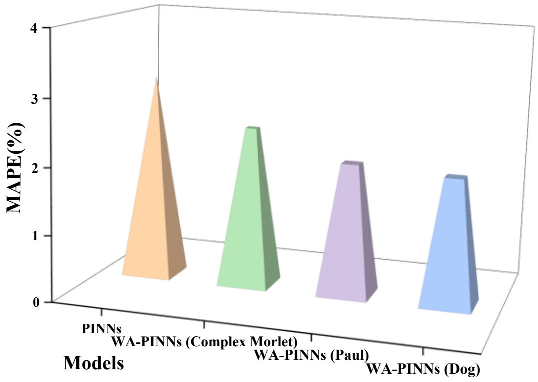

(c) MAPE

Figure 16. Prediction errors of the average diameters in scheme B compared with field experiments.

4.4.2. Prediction results of volume

To further validate the accuracy of the proposed method, the volume of the blasting crater is also predicted. The corresponding results of the six methods under the two schemes are presented in Tables 13 and 14 and Figure 17.

Table 13. The volume of blasting craters utilizing six methods in scheme A.

Charge mass	3kg	4 kg	5 kg	6 kg
Numerical simulation/(m^3)	1.4510	4.1104	6.2867	10.1089
Field experiment/(m^3)	1.6965	3.8170	6.5408	10.5975
PINNs/ m^3)	1.5538	3.9561	6.4124	10.3952
WA-PINNs (Complex Morlet) /(m^3)	1.5428	4.2088	6.3977	10.3761
WA-PINNs (Paul) /(m^3)	1.4317	4.1007	6.3865	10.2688
WA-PINNs (Dog) /(m^3)	1.4433	4.1203	6.1736	10.1134

Table 14. The volume of blasting craters utilizing six methods in scheme B.

Burial depth	1.4m	1.6m	1.8m	2.0m
Numerical simulation/(m^3)	4.6332	5.4687	4.2029	2.9847
Field experiment/(m^3)	4.5743	5.3147	3.6945	3.0159
PINNs/ m^3)	4.4825	5.3348	3.7540	2.9626
WA-PINNs (Complex Morlet) /(m^3)	4.5422	5.3249	3.7426	2.9681
WA-PINNs (Paul) /(m^3)	4.6173	5.3563	3.9455	2.9786
WA-PINNs (Dog) /(m^3)	4.6418	5.4076	4.1533	2.9914

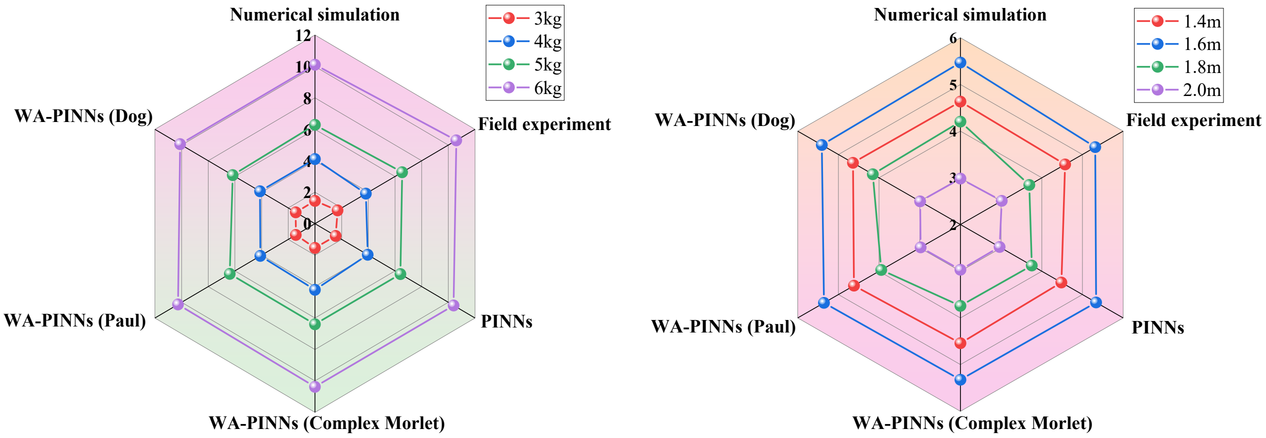

(a) Volume of scheme A

(b) Volume of scheme B

Figure 17. The volumes of two schemes.

For the volume in scheme A, compared to the numerical simulation results (shown in Figure 18), the MAE values of the four models, the PINNs model, WA-PINNs (Complex Morlet) model, WA-PINNs (Paul) model, and WA-PINNs (Dog) model, are 0.1673m^3, 0.1421m^3, 0.0722m^3, and 0.0338m^3, respectively; the RMSE values are 0.182 m^3, 0.160 m^3, 0.095 m^3, and 0.057 m^3, respectively; and the MAPE values are 3.92%, 3.28%, 1.18%, and 0.65%, respectively. Compared to the PINNs method, the MAE values of the three models, WA-PINNs (Complex Morlet), WA-PINNs (Paul), and WA-PINNs (Dog), are reduced by 79.8%, 36.2%, and 53.2%, respectively; the RMSE values are reduced by 68.68%, 64.38%, and 40%, respectively; and the MAPE values are reduced by 83.42%, 80.18%, and 44.92%, respectively.

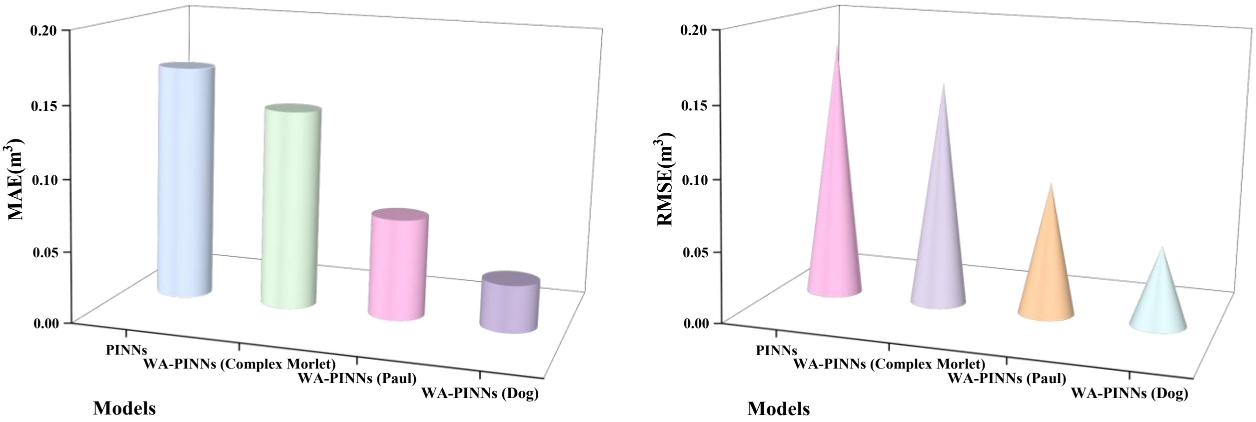

(a) MAE (b) RMSE

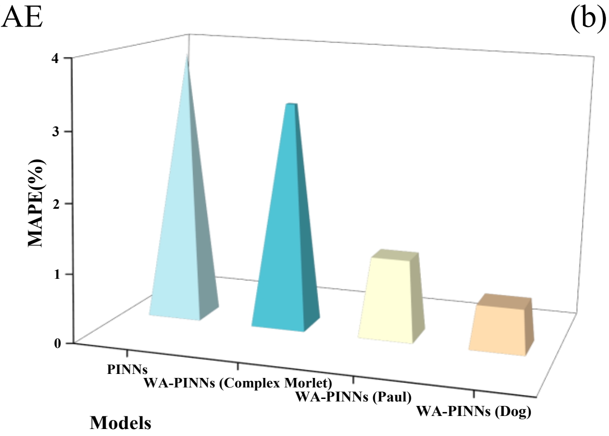

(c) MAPE

Figure 18. Prediction errors of the volume in scheme A compared with numerical simulations.

For the volume in scheme A, compared to the field experiment results (shown in Figure 19), the MAE values of the four models, PINNs model, WA-PINNs (Complex Morlet) model, WA-PINNs (Paul) model, and WA-PINNs (Dog) model, are 0.1531m^3, 0.2275m^3, 0.2579 m^3, and 0.3520 m^3, respectively; the RMSE values are 0.1558 m^3, 0.2483 m^3, 0.2657 m^3, and 0.3624 m^3, respectively; and the MAPE values are 3.98%, 5.90%, 7.13%, and 8.27%, respectively. Unlike the previous results, the predictive performance of the four models ranks as follows: PINNs > WA-PINNs (Complex Morelet) > WA-PINNs (Paul) > WA-PINNs (Dog).

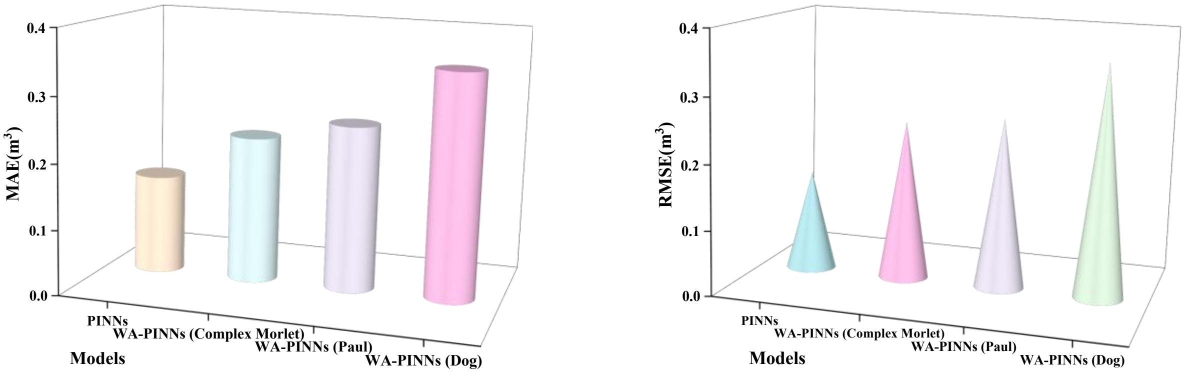

(a) MAE (b) RMSE

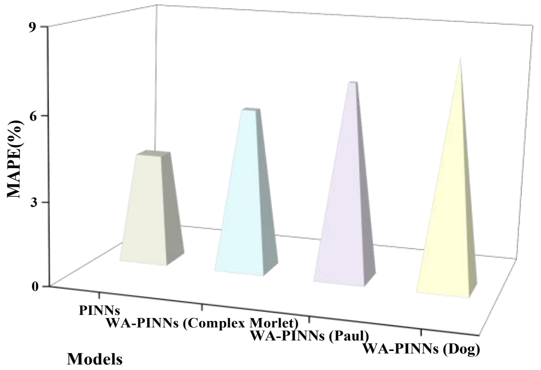

(c) MAPE

Figure 19. Prediction errors of the volume in scheme A compared with field experiments.

For the volume in scheme B, compared to the field experiment results (shown in Figure 20), the MAE values of the four models, the PINNs model, WA-PINNs (Complex Morlet) model, WA-PINNs (Paul) model, and WA-PINNs (Dog) model, are 0.1889m^3, 0.1779 m^3, 0.0980 m^3, and 0.0315 m^3, respectively; the RMSE values are 0.2463 m^3, 0.2455 m^3, 0.1407 m^3, and 0.0397m^3, respectively; and the MAPE values are 4.28%, 4.03%, 2.18%, and 0.68%, respectively. Unlike the previous results, the predictive performance of the four models ranks as follows: PINNs > WA-PINNs (Complex Morelet) > WA-PINNs (Paul) > WA-PINNs (Dog).

For the volume in scheme B, compared to the field experiment results (shown in Figure 21), the MAE values of the four models, the PINNs model, WA-PINNs (Complex Morlet) model, WA-PINNs (Paul) model, and WA-PINNs (Dog) model, are 0.0562m^3, 0.0346 m^3, 0.0932 m^3, and 0.1609 m^3, respectively; the RMSE values are 0.0585 m^3, 0.0367 m^3, 0.1307 m^3, and 0.2389 m^3, respectively; and the MAPE values are 1.44%, 0.94%, 2.44 %, and 4.11%, respectively. Unlike the previous results, the predictive performance of the four models ranks as follows: WA-PINNs (Complex Morelet) > PINNs > WA-PINNs (Paul) > WA-PINNs (Dog).

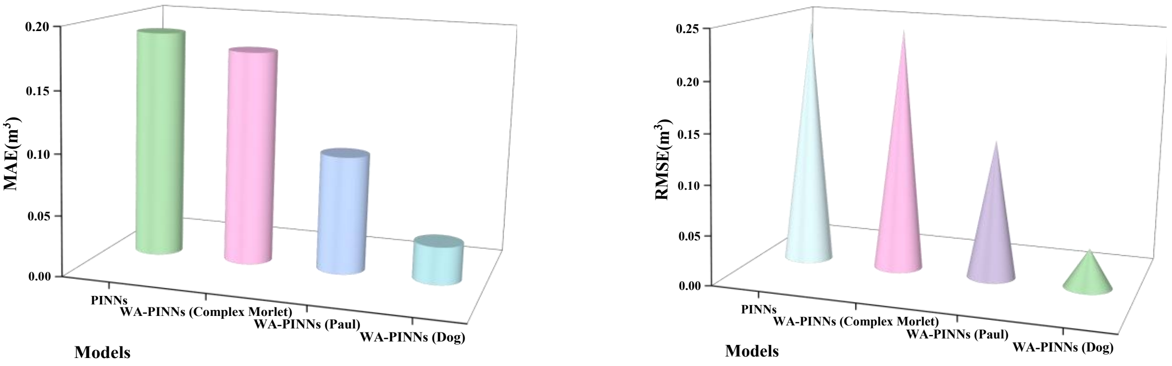

(a) MAE (b) RMSE

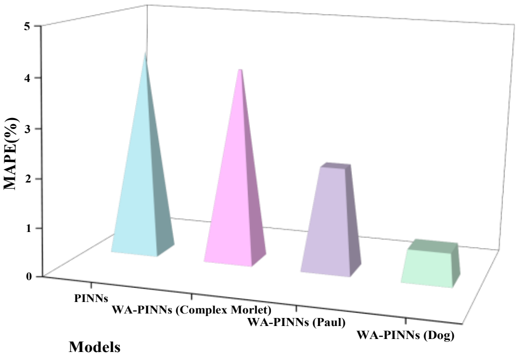

(c) MAPE

Figure 20. Prediction errors of the volume in scheme B compared with numerical simulations.

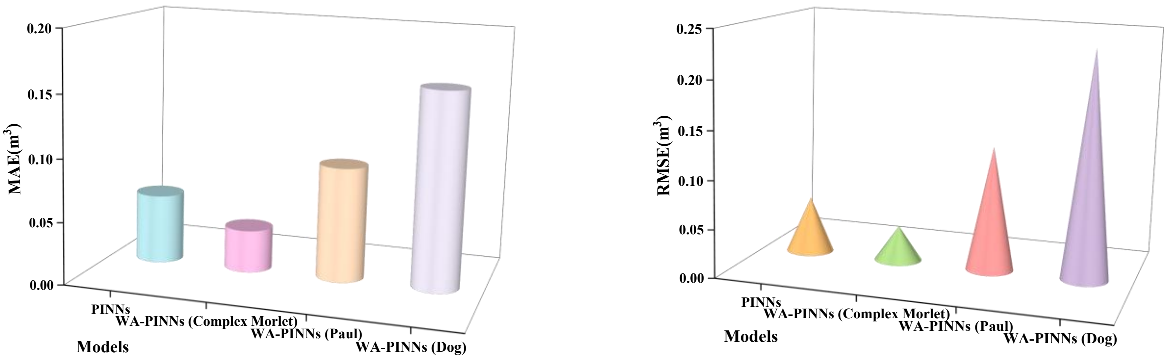

(a) MAE (b) RMSE

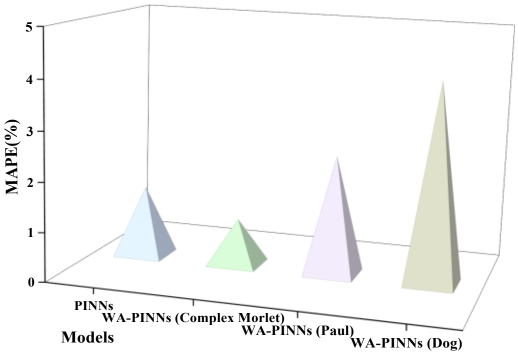

(c) MAPE

Figure 21. Prediction errors of the volume in scheme B compared with field experiments.

5. Conclusions

Aiming to manage the limitations of traditional methods in the calculation of cylindrical blasthole blasting crater, we construct a WA-PINNs-based intelligent solution model by combining the blast load equivalence principle, Starfield superposition algorithm, and wavelet enhanced neural network, and verify, the effectiveness and superiority of the model through theoretical derivation, numerical simulation and field experiments. The following four critical conclusions can be drawn and highlighted:

(1) The established cylindrical-spherical charge equivalent model based on the blast load equivalence principle and Starfield superposition algorithm can accurately characterize the stress wave propagation and superposition law of cylindrical charges by decomposing them into multiple spherical charges. Moreover, the constructed partial differential equation solution model for the blasting crater range provides a rigorous physical basis for the subsequent intelligent calculation of blasting crater geometric parameters, which makes up for the deficiency of idealized assumptions in traditional theoretical calculation methods.

(2) The proposed WA-PINNs framework effectively solves the problems of high computational overhead and poor adaptability to high-gradient problems of traditional PINNs. By introducing wavelet basis functions and optimizing expansion coefficients, the model avoids the difficulty of balancing loss components in automatic differentiation, and the integration of multi-scale wavelet analysis enables the model to capture the local and global characteristics of blasting stress wave propagation and rock fracture more accurately. Among the three wavelet functions, the Dog wavelet function has the best matching degree with the blasting engineering problem, and the corresponding WA-PINNs model shows the highest prediction accuracy and the shortest training time.

(3) Numerical simulation and field experiment results confirm that the WA-PINNs model has significant advantages in the prediction of blasting crater diameter and volume compared with the traditional PINNs model. For the diameter prediction, the relative error of the WA-PINNs (Dog) model is as low as 0.01, and the MAE, RMSE, and MAPE are far lower than those of the traditional PINNs model, and the prediction results are highly consistent with the actual measured values. For the volume prediction, the WA-PINNs model can effectively capture the change law of blasting crater volume with charge mass and burial depth, and the error indices are controlled within a reasonable range, which solves the problem of poor prediction stability of traditional data-driven neural networks in engineering applications.

(4) The change law of blasting crater geometric parameters revealed by the experiment is consistent with the engineering practice: The diameter and volume of the blasting crater increase with the increase of charge mass under the fixed burial depth; under the fixed charge mass, the diameter and volume of the blasting crater first increase and then decrease with the increase of burial depth, and the optimal burial depth exists to maximize the blasting crater range. The WA-PINNs model can accurately fit this change law, which provides a reliable theoretical basis for the selection of optimal charge parameters in actual blasting engineering.

In summary, the WA-PINNs-based intelligent calculation method for cylindrical blasthole blasting craters proposed in this study realizes the organic combination of blasting engineering physical mechanisms and intelligent computing, which not only improves the accuracy and efficiency of blasting crater parameter prediction, but also provides a new research idea for the intelligent analysis of other blasting engineering problems such as blast-induced vibration and rock fragmentation optimization. In follow-up research, the model can be further optimized by introducing more complex geological factors (such as rock joint development, in-situ stress field) and expanding the sample size of field experiments. Moreover, the application scope of the model can be extended to bench blasting, tunnel blasting, and other engineering scenarios to provide more comprehensive technical support for the intelligent and precise design of blasting engineering.

Author contributions

Ting Zhu-Investigation; Methodology; Project administration; Resources; Software; Supervision; Validation; Visualization; Hongyu Zhang-Investigation; Methodology; Yongsheng Jia-Funding acquisition; Yingkang Yao-Funding acquisition; Fan Yong-Methodology; Jinshan Sun-Funding acquisition; Formal analysis; Methodology; Writing-review & editing; Nan Jiang-Funding acquisition.

Use of Generative-AI tools declaration

The author declares they have not used Artificial Intelligence (AI) tools in the creation of this article.

Acknowledgments

This research is supported by the State Key Program of National Natural Science of China (Grant No.U25A20355);the Central Government-guided Local Science and Technology Development Special Project of Hubei Province (No.2025CSA141;NO.2025CSA014); Chutian Talent Program Special Project for Innovation and Entrepreneurship Teams of Hubei (2024;2025);the key Research and Development Program of Wuhan (2024050802030155); the Doctor initiated Fund of State Key Laboratory of Precision Blasting[PBSKL-2025-QD-12]; Hubei Provincial Key Laboratory of Metallurgical Industry Process System Science(No. Y202401) ; the "111 Center" (No. D25004).

Conflict of interest

The author declares no conflict of interest in this paper.

References

1. A. Khodayari, C. Xu, P. Dare-Bryan, P. Dowd, V. Lapcevic, A. Metcalfe, Impact of blast design parameters on rock fragmentation in sub-level caving: A multivariate regression approach, *J. Rock Mech. Geotech. Eng.*, 2025. In press. https://doi.org/10.1016/j.jrmge.2025.07.038
2. J. Li, W. Wu, B. Pan, B. Dong, H. Zhu, Impact of joint distribution within hard rock mass on tunnel blasting profile: Numerical simulation and field measurement, *J. Rock Mech. Geotech. Eng.*, 2025. In press. https://doi.org/10.1016/j.jrmge.2025.06.032
3. L. Ji, C. Zhou, N. Jiang, X. Meng, A theoretical model to predict blast-induced vibration and its zoning characteristics in surrounding rock of a tunnel, *Tunn. Undergr. Sp. Tech.*, **162** (2025), 106650. https://doi.org/10.1016/j.tust.2025.106650.

4. X. Wang, C. Liu, B. Liu, F. Zhang, S. Cui, X. Wang, et al., Mechanism of formation of blasting craters and evolution of its characteristic parameters under in-situ stress, *Eng. Geol.*, **351** (2025), 108028. https://doi.org/10.1016/j.enggeo.2025.108028.
5. Y. Ning, J. Yang, X. An, G. Ma, Modelling rock fracturing and blast-induced rock mass failure via advanced discretisation within the discontinuous deformation analysis framework, *Comput. Geotech.*, **38** (2011), 40–49. https://doi.org/10.1016/j.compgeo.2010.09.003
6. P. Yan, W. Zhou, W. Lu, M. Chen, C. Zhou, Simulation of bench blasting considering fragmentation size distribution, *Int. J. Impact Eng.*, **90** (2016), 132–145. https://doi.org/10.1016/j.ijimpeng.2015.11.015
7. Z. Zhang, W. Gao, K. Li, B. Li, Numerical simulation of rock mass blasting using particle flow code and particle expansion loading algorithm, *Simul. Model. Pract. Th.*, **104** (2020), 102119. https://doi.org/10.1016/j.simpat.2020.102119
8. W. Gao, Z. Zhang, B. Li, K. Li, Study on numerical simulation of geometric elements of blasting funnel based on PFC5.0, *Shock Vib.*, **2021** (2021), 8812964. https://doi.org/10.1155/2021/8812964
9. Z. L. Wang, H. Konietzky, Modelling of blast-induced fractures in jointed rock masses, *Eng. Fract. Mech.*, **76** (2009), 1945–1955. https://doi.org/10.1016/j.engfracmech.2009.05.004
10. Z. L. Wang, Y. C. Li, R. F. Shen, Numerical simulation of tensile damage and blast crater in brittle rock due to underground explosion, *Int. J. Rock Mech. Min. Sci.*, **44** (2007), 730–738. https://doi.org/10.1016/j.ijrmms.2006.11.004
11. Z. Wang, H. Wang, J. Wang, N. Tian, Finite element analyses of constitutive models performance in the simulation of blast-induced rock cracks, *Comput. Geotech.*, **135** (2021), 104172. https://doi.org/10.1016/j.compgeo.2021.104172
12. Z. Zhu, Numerical prediction of crater blasting and bench blasting, *Int. J. Rock Mech. Min. Sci.*, **46** (2009), 1088–1096. https://doi.org/10.1016/j.ijrmms.2009.05.009
13. Z. Zhu, B. Mohanty, H. Xie, Numerical investigation of blasting-induced crack initiation and propagation in rocks, *Int. J. Rock Mech. Min. Sci.*, **44** (2007), 412–424. https://doi.org/10.1016/j.ijrmms.2006.09.002
14. Z. Zhu, H. Xie, B. Mohanty, Numerical investigation of blasting-induced damage in cylindrical rocks, *Int. J. Rock Mech. Min. Sci.*, **45** (2008), 111–121. https://doi.org/10.1016/j.ijrmms.2007.04.012
15. T. Q. Ye, Field experiment for blasting crater, *J. China Univ. Min. Technol.*, **18** (2008), 224–228. https://doi.org/10.1016/s1006-1266(08)60047-4
16. V. Hassija, V. Chamola, A. Mahapatra, A. Singal, D. Goel, K. Huang, et al., Interpreting black-box models: a review on explainable artificial intelligence, *Cogn. Comput.*, **16** (2024), 45–74. https://doi.org/10.1007/s12559-023-10179-8
17. M. Zhao, J. Liu, H. Zheng, L. Wang, Contrast reconstruction of overfilled cavities by incorporating multi-frequency scattering fields and attention mechanism into two-step learning method, *Eng. Anal. Boundary Elem.*, **166** (2024), 105813. https://doi.org/10.1016/j.enganabound.2024.105813
18. M. Hojjat, S. G. Etemad, R. Bagheri, J. Thibault, Thermal conductivity of non-Newtonian nanofluids: experimental data and modeling using neural network, *Int. J. Heat Mass Transfer*, **54** (2011), 1017–1023. https://doi.org/10.1016/j.ijheatmasstransfer.2010.11.039

19. S. L. Hung, C. S. Huang, C. Wen, Y. Hsu, Nonparametric identification of a building structure from experimental data using wavelet neural network, *Comput.-Aided Civ. Inf.*, **18** (2003), 356–368. https://doi.org/10.1111/1467-8667.t01-1-00313
20. Z. Shah, M. A. Z. Raja, Y. M. Chu, W. A. Khan, M. Waqas, M. Shoaib, et al., Design of neural network based intelligent computing for neumerical treatment of unsteady 3D flow of Eyring-Powell magneto-nanofluidic model, *J. Mater. Res. Technol.*, **9** (2020), 14372–14387. https://doi.org/10.1016/j.jmrt.2020.09.098
21. M. Raissi, P. Perdikaris, G. E. Karniadakis, Physics-informed neural networks: a deep learning framework for solving forward and inverse problems involving nonlinear partial differential equations, *J. Comput. Phys.*, **378** (2019), 686–707. https://doi.org/10.1016/j.jcp.2018.10.045
22. X. Jin, S. Cai, H. Li, G. E. Karniadakis, NSFnets (Navier-Stokes flow nets): physics-informed neural networks for the incompressible Navier-Stokes equations, *J. Comput. Phys.*, **426** (2021), 109951. https://doi.org/10.1016/j.jcp.2020.109951
23. Z. Mao, A. D. Jagtap, G. E. Karniadakis, Physics-informed neural networks for high-speed flows, *Comput. Method. Appl. Mech. Eng.*, **360** (2020), 112789. https://doi.org/10.1016/j.cma.2019.112789
24. S. Cuomo, V. S. Di Cola, F. Giampaolo, G. Rozza, M. Raissi, F. Piccialli, Scientific machine learning through physics-informed neural networks: Where we are and what's next, *J. Sci. Comput.*, **92** (2022), 88. https://doi.org/10.1007/s10915-022-01939-z
25. M. Delcey, Y. Cheny, J. B. Keck, A. Gans, S. K. De Richter, Identification of settling velocity with physics informed neural networks for sediment laden flows, *Comput. Method. Appl. Mech. Eng.*, **432** (2024), 117389. https://doi.org/10.1016/j.cma.2024.117389
26. A. K. Sarma, S. Roy, C. Annavarapu, P. Roy, S. Jagannathan, Interface PINNs (I-PINNs): A physics-informed neural networks framework for interface problems, *Comput. Methods Appl. Mech. Eng.*, **429** (2024), 117135. https://doi.org/10.1016/j.cma.2024.117135
27. S. Cai, Z. Mao, Z. Wang, M. Yin, G. E. Karniadakis, Physics-informed neural networks (PINNs) for fluid mechanics: A review, *Acta Mech. Sin.*, **37** (2021), 1727–1738. https://doi.org/10.1007/s10409-021-01148-1
28. H. Wessels, C. Weißenfels, P. Wriggers, The neural particle method-an updated Lagrangian physics informed neural network for computational fluid dynamics, *Comput. Method. Appl. Mech. Eng.*, **368** (2020), 113127. https://doi.org/10.1016/j.cma.2020.113127
29. Y. Gu, L. Xie, W. Qu, S. Zhao, Interface crack analysis in 2D bounded dissimilar materials using an enriched physics-informed neural networks, *Eng. Anal. Bound. Elem.*, **163** (2024), 465–473. https://doi.org/10.1016/j.enganabound.2024.03.030
30. A. D. Jagtap, Z. Mao, N. Adams, G. E. Karniadakis, Physics-informed neural networks for inverse problems in supersonic flows, *J. Comput. Phys.*, **466** (2022), 111402. https://doi.org/10.1016/j.jcp.2022.111402
31. L. D. McClenny, U. M. Braga-Neto, Self-adaptive physics-informed neural networks, *J. Comput. Phys.*, **474** (2023), 111722. https://doi.org/10.1016/j.jcp.2022.111722
32. Y. Wang, Y. Yao, J. Guo, Z. Gao, A practical PINN framework for multi-scale problems with multi-magnitude loss terms, *J. Comput. Phys.*, **510** (2024), 113112. https://doi.org/10.1016/j.jcp.2024.113112

33. S. Yin, Z. Xiang, Adaptive collision avoidance strategy for USVs in perception-limited environments using dynamic priority guidance, *Adv. Eng. Inform.*, **65** (2025), 103355. https://doi.org/10.1016/j.aei.2025.103355
34. S. Yin, Z. Xiang, ADE-MIFS: Real-time cooperative navigation for multi-USVs in dynamic maritime environments, *Ocean Eng.*, **352** (2026), 124487. https://doi.org/10.1016/j.oceaneng.2026.124487
35. A. G. Baydin, B. A. Pearlmutter, A. A. Radul, J. M. Siskind, Automatic differentiation in machine learning: A survey, *J. Mach. Learn. Res.*, **18** (2018), 1–43.
36. H. Pandey, A. Singh, R. Behera, An efficient wavelet-based physics-informed neural networks for singularly perturbed problems, 2024, arXiv: 2409.11847. https://doi.org/10.48550/arXiv.2409.11847
37. Y. Fan, J. G. Wu, Z. D. Leng, G. D. Yang, X. Z. Cui, Experiment and simulation of rock fragmentation size of blasting crater, *J. Rock Mech. Eng.*, **42** (2023), 2125–2139. In Chinese. https://doi.org/10.13722/j.cnki.jrme.2022.0869

AIMS Press